

Deep Algorithm Unrolling for Biomedical Imaging

Yuelong Li, Or Bar-Shira, Vishal Monga and Yonina C. Eldar

1 Deep Algorithm Unrolling for Biomedical Imaging

1.1 Introduction

Model-based inversion has played a dominant role in biomedical imaging prior to deep learning gaining widespread popularity and broad recognition. Model-based techniques rely on a *forward model* derived by modeling the imaging process analytically based on physical laws. Typically, the forward model is formulated as:

$$\mathbf{y} = \mathcal{F}(\mathbf{x}) + \mathbf{n},$$

where $\mathbf{y} \in \mathbb{R}^m$ is the observation, $\mathbf{x} \in \mathbb{R}^n$ is the underlying image data to be recovered, \mathcal{F} is the mapping from image domain to observations, and $\mathbf{n} \in \mathbb{R}^m$ is the corruptive noise process.

Under many circumstances, the problem of estimating \mathbf{x} from \mathbf{y} is ill-posed, because the imaging process is often compressive due to practical constraints (Eldar & Kutyniok 2012a). For instance, in Medical Resonance Imaging (MRI) one may undersample the image in order to accelerate the acquisition process; in Computed Tomography (CT) a reduction of dose through sparse views in X-ray radiation is generally preferred for patients' safety which translates into an underdetermined forward model. Therefore, to reliably estimate \mathbf{x} , a prior structure is often incorporated either by capturing physical principles or through manual handcrafting. The underlying image \mathbf{x} can then be estimated by solving a regularized optimization problem:

$$\min_{\mathbf{x}} \rho(\mathbf{y}, \mathcal{F}(\mathbf{x})) + \lambda \mathcal{R}(\mathbf{x}), \quad (1.1)$$

where ρ is a metric measuring the deviation in the measurements, \mathcal{R} is a regularization functional capturing prior structure, and λ is a regularization parameter controlling the regularization strength. Problem (1.1) is generally solved via an iterative optimization algorithm.

In contrast to the model-based framework, \mathbf{x} can alternatively be estimated by learning a regression mapping from \mathbf{y} (or its transformed version such as compressive samples or Fourier coefficients) to \mathbf{x} through a data-driven approach. The regression mapping can be chosen from various machine learning models, among which Deep Neural Networks (DNN) are increasingly popular nowadays. In particular, a purely data-driven approach adopts a generic DNN without

incorporating any physical laws or prior structure. Instead, it relies on abundant training data to learn a huge number of network parameters, and in turn the form of the regression mapping. When the training data is adequate, this approach can be highly successful because DNNs are extremely expressive and can learn to adapt towards complicated mappings which are difficult to characterize and design manually. In addition, with the aid of highly optimized deep learning platforms and hardware accelerators such as Graphics Processing Units (GPU), inference via DNN can be performed rapidly, which gives rise to fast execution speed in practice. This is in contrast with traditional iterative algorithms which need to repeat certain operations a large number of times sequentially, and can be quite slow comparatively.

Nevertheless, modern DNNs typically carry a deep hierarchical architecture composed of many layers and network parameters (can be millions) and are thus often difficult to interpret. It is hard to discover what is the exact form that is learned by the DNNs and what are the roles of the individual parameters. In other words, DNNs, as an intact machine learning system, generally lacks the ability for humans to disintegrate, analyze and draw analogies. The ability to understand the sequence of operations of a trained learning system that allows the manipulation of its inner mechanism in a principled, predictable fashion is commonly referred to as *interpretability*. Lack of interpretability is an important concern as it is usually the key to conceptual understanding and advancing knowledge frontiers. In addition, in practical biomedical applications, interpretability is key to ensure trust in the reconstruction algorithm, as experts need to have proper understanding of the origin of the artifacts introduced by the algorithm and identify potential failure cases (Min, Lee & Yoon 2017). In contrast, traditional iterative algorithms are usually highly interpretable because they are developed via modeling underlying physical processes and/or capturing prior domain knowledge.

In addition to interpretability, generalizability is another fundamental requirement in biomedical applications. It is well known that generic DNNs heavily rely on the quantity and quality of training data in order to achieve empirically superior performance. In other words, when training data is deficient, the issue of over-fitting may manifest itself in the form of significantly degraded network performance. Indeed, this issue can be so serious that the DNNs may underperform traditional iterative algorithms. This phenomenon is especially apparent for DNNs with high model capacity, such as very deep or ultra wide neural networks. Unlike natural images, in biomedical imaging the data collection is an expensive and time-consuming procedure, and thus generalizability is especially important.

In the seminal work of Gregor and LeCun (Gregor & LeCun 2010), a promising technique called algorithm unrolling was developed that has helped connect iterative algorithms such as sparse coding techniques to DNNs. This work has inspired a growing list of follow-ups in different fields of biomedical research: Compressive Sensing (CS) (Yang, Sun, Li & Xu 2018), Computed Tomogra-

phy (CT) (Hauptmann, Lucka, Betcke, Huynh, Adler, Cox, Beard, Ourselin & Arridge 2018), Ultrasound (Solomon, Cohen, Zhang, Yang, He, Luo, van Sloun & Eldar 2020, Mischi, Bell, van Sloun & Eldar 2020), to name a few. Figure 1.1 provides a high-level illustration of this framework. Starting with an iterative procedure, each iteration of the algorithm is represented as one layer of a network. Concatenating these layers forms a deep neural network whose architecture borrows from the optimization method. Passing through the network is equivalent to executing the iterative algorithm a finite number of times. In addition, the algorithm parameters (such as the model parameters and regularization coefficients) transfer to the network parameters. The network may be trained using back-propagation resulting in model parameters that are learned from real world training sets. In this way, the trained network can be naturally interpreted as a parameter optimized algorithm, effectively overcoming the lack of interpretability in most conventional neural networks (Monga, Li & Eldar 2019).

Traditional iterative algorithms generally entail significantly fewer parameters compared with popular neural networks. Therefore, the unrolled networks are highly parameter efficient and require less training data. In addition, unrolled networks naturally inherit prior structure and domain knowledge rather than learn them from intensive training data. Consequently, they tend to generalize better than generic networks, and can be computationally faster as long as each algorithmic iteration (or the corresponding layer) is not overly expensive.

In this chapter, we review biomedical applications and breakthroughs via leveraging algorithm unrolling, an important technique that bridges between traditional iterative algorithms and modern deep learning techniques. To provide context, we start by tracing the origin of algorithm unrolling and providing a comprehensive tutorial on how to unroll iterative algorithms into deep networks. We then extensively cover algorithm unrolling in a wide variety of biomedical imaging modalities and delve into several representative recent works in detail. Indeed, there is a rich history of iterative algorithms for biomedical image synthesis, which makes the field ripe for unrolling techniques. In addition, we put algorithm unrolling into a broad perspective, in order to understand why it is particularly effective and discuss recent trends. Finally, we conclude the chapter by discussing open challenges, and suggesting future research directions.

1.2 Development of Algorithm Unrolling

This section introduces algorithm unrolling. We begin by reviewing Learned Iterative Shrinkage and Thresholding Algorithm (LISTA), the first work that employs the algorithm unrolling strategy. To this end, we review the classical Iterative Shrinkage and Thresholding Algorithm (ISTA) (Section 1.2.1), and then discuss how it can be unrolled into a deep network (Section 1.2.2). Next we consider several related theoretical studies to gain a deeper understanding of LISTA

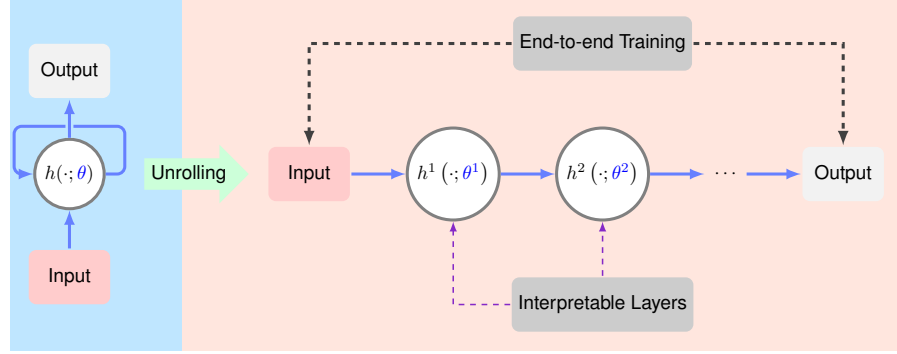


Figure 1.1 A high-level overview of algorithm unrolling: given an iterative algorithm (left), a corresponding deep network (right) can be generated by cascading its iterations h . The iteration step h (left) is executed a number of times, resulting in the network layers h^1, h^2, \dots (right). Each iteration h depends on algorithm parameters θ , which are transferred into network parameters $\theta^1, \theta^2, \dots$ and learned from training datasets through end-to-end training. In this way, the resulting network could achieve better performance than the original iterative algorithm. In addition, the network layers naturally inherit interpretability from the iteration procedure. The learnable parameters are colored in blue.

(Section 1.2.3). We then introduce the general idea of algorithm unrolling in an abstract fashion and extend it to generic iterative algorithms (Section 1.2.4).

1.2.1 Iterative Shrinkage and Thresholding Algorithm

In many practical problems, the signal of interest cannot be observed directly, but must be inferred from observable quantities. In the simplest approximation, which often suffices, there is a linear relationship between the signal of interest and the observed quantities (Daubechies, Defrise & De Mol 2004). If we model the signal of interest by a vector \mathbf{x} , and the derived quantities by another vector \mathbf{y} , we can cast the problem of inferring \mathbf{x} from \mathbf{y} as a linear inverse problem. A basic linear inverse problem admits the following form:

$$\mathbf{y} = \mathbf{A}\mathbf{x} + \mathbf{n}, \quad (1.2)$$

where $\mathbf{A} \in \mathbb{R}^{n \times m}$ and $\mathbf{y} \in \mathbb{R}^n$ are known, \mathbf{n} is an unknown noise vector, and \mathbf{x} is the unknown signal of interest to be estimated.

In practice, it is often the case that \mathbf{A} has fewer rows than columns ($n < m$) so that recovery of \mathbf{x} from \mathbf{y} becomes an ill-posed problem. It is therefore impossible to recover \mathbf{x} without introducing additional assumptions on its structure. A popular strategy is to assume that \mathbf{x} is sparse or admits a compressible (sparse) representation, meaning it is sparse in a transformed domain (Eldar & Kutyniok 2012a).

In sparse coding, we seek a vector $\mathbf{x} \in \mathbb{R}^m$ such that $\mathbf{y} \approx \mathbf{W}\mathbf{x}$ while encouraging as many coefficients in \mathbf{x} to be zero (or small in magnitude) as possible (Chen, Donoho & Saunders 2001). Here \mathbf{W} is commonly called a *dictionary* whose columns, typically named *atoms*, can either be from a standard basis (or frames) such as Fourier or wavelet basis, or be learned from real data. A popular technique to recover \mathbf{x} is by solving an unconstrained convex minimization problem:

$$\min_{\mathbf{x} \in \mathbb{R}^m} \frac{1}{2} \|\mathbf{y} - \mathbf{W}\mathbf{x}\|_2^2 + \lambda \|\mathbf{x}\|_1, \quad (1.3)$$

where $\lambda > 0$ is a regularization parameter that controls the sparsity of the solution. A well known class of methods for solving (1.3) are proximal methods such as ISTA (Daubechies et al. 2004), which perform the following iterations:

$$\mathbf{x}^{l+1} = \mathcal{S}_\lambda \left\{ \left(\mathbf{I} - \frac{1}{\mu} \mathbf{W}^T \mathbf{W} \right) \mathbf{x}^l + \frac{1}{\mu} \mathbf{W}^T \mathbf{y} \right\}, \quad l = 0, 1, \dots \quad (1.4)$$

Here, $\mathbf{I} \in \mathbb{R}^{m \times m}$ is the identity matrix, μ is a positive parameter that controls the iteration step size, $\mathcal{S}_\lambda(\cdot)$ is the soft-thresholding operator defined as

$$\mathcal{S}_\lambda(x) = \text{sign}(x) \cdot \max\{|x| - \lambda, 0\}, \quad (1.5)$$

for a scalar x , and $\mathcal{S}_\lambda(\cdot)$ operates element-wise on vectors and matrices.

1.2.2 LISTA: Learned Iterative Shrinkage and Thresholding Algorithm

The slow convergence rate of ISTA can be problematic in real-time applications. Furthermore, the matrix \mathbf{W} may not be known exactly. In their seminal work, Gregor *et al.* propose a highly efficient learning-based method that computes good approximations of optimal sparse codes in a fixed amount of time, with the help of \mathbf{W} learned from real data (Gregor & LeCun 2010).

Specifically, the authors develop deep algorithm unrolling as a strategy for designing neural networks which integrate domain knowledge. In this approach, the network architecture is tailored to a specific problem, based on a well-founded iterative mathematical formulation for solving the problem at hand. This leads to increased convergence speed and accuracy with respect to the standard iterative solution, and interpretability and robustness relative to a black-box large-scale neural network.

To unroll ISTA, iteration (1.4) can be recast into a single network layer as depicted in Fig. 1.2. This layer comprises a series of analytical operations (matrix-vector multiplication, summation, soft-thresholding), which is of the same nature as a neural network. A diagram representation of one iteration step reveals its resemblance to a single network layer. Executing ISTA L times can be interpreted as cascading L such layers, which essentially forms an L -layer deep network. Note that, in the unrolled network an implicit substitution of parameters has been made: $\mathbf{W}_t = \mathbf{I} - \frac{1}{\mu} \mathbf{W}^T \mathbf{W}$ and $\mathbf{W}_e = \frac{1}{\mu} \mathbf{W}^T$.

After unrolling ISTA into a network, named Learned ISTA (LISTA), the network is trained through back-propagation using real datasets to optimize the parameters \mathbf{W}_t , \mathbf{W}_e and λ . Training is performed in a supervised manner, meaning that for every input vector $\mathbf{y}^t \in \mathbb{R}^n, t = 1, \dots, T$, its corresponding sparse output $\mathbf{x}^{*t} \in \mathbb{R}^m, t = 1, \dots, T$ is known (by choosing an appropriate λ which is fixed and might be different from the learned value). The sparse codes \mathbf{x}^{*t} can be determined, for example, by executing ISTA when \mathbf{W} is known. Inputting the vector \mathbf{y}^t into the network results in a predicted output $\hat{\mathbf{x}}^t(\mathbf{y}^t; \mathbf{W}_t, \mathbf{W}_e, \lambda)$. The network training loss function is formed by comparing the prediction with the known sparse output \mathbf{x}^{*t} :

$$\ell(\mathbf{W}_t, \mathbf{W}_e, \lambda) = \frac{1}{T} \sum_{t=1}^T \|\hat{\mathbf{x}}^t(\mathbf{y}^t; \mathbf{W}_t, \mathbf{W}_e, \lambda) - \mathbf{x}^{*t}\|_2^2. \quad (1.6)$$

The network is trained through loss minimization, using popular gradient-based learning techniques such as stochastic gradient descent, to learn the unknown parameters \mathbf{W}_t , \mathbf{W}_e and λ (LeCun, Bottou, Orr & Müller 2012).

The learned version, LISTA, may achieve higher efficiency compared to ISTA. It is also useful when it is analytically hard to determine \mathbf{W} . Furthermore, it has been shown empirically that, the number of layers L in (trained) LISTA can be an order of magnitude smaller than the number of iterations required for ISTA to achieve convergence corresponding to a new observed input, thus dramatically boosting the sparse coding efficiency (Gregor & LeCun 2010). In practice, \mathbf{W}_t , \mathbf{W}_e and λ can be untied and vary in each layer.

1.2.3 Towards Theoretical Understanding of Algorithm Unrolling

While LISTA empirically achieves much higher efficiency compared to ISTA, theoretical understanding of its behavior is still lacking. In particular, conditions offering convergence guarantees, rates of convergence, structure of the optimal solutions, factors contributing to higher empirical performance, are some of the important problems that need to be answered. In recent years, researchers have actively analyzed LISTA and its variants and made significant progress.

Xin *et al.* (Xin, Wang, Gao, Wipf & Wang 2016) study the unrolled Iterative Hard Thresholding (IHT) algorithm, which has been widely applied in various sparsity constrained estimation problems. IHT largely resembles ISTA except that an ℓ^0 norm is employed instead of the ℓ^1 norm. Formally, IHT solves the following optimization problem instead of (1.3):

$$\min_{\mathbf{x} \in \mathbb{R}^m} \frac{1}{2} \|\mathbf{y} - \mathbf{W}\mathbf{x}\|_2^2 \quad \text{subject to} \quad \|\mathbf{x}\|_0 \leq k, \quad (1.7)$$

for some positive integer k . IHT essentially performs the following iterations:

$$\mathbf{x}^{l+1} = \mathcal{H}_k \left\{ \left(\mathbf{I} - \frac{1}{\mu} \mathbf{W}^T \mathbf{W} \right) \mathbf{x}^l + \frac{1}{\mu} \mathbf{W}^T \mathbf{y} \right\}, \quad l = 0, 1, \dots, \quad (1.8)$$

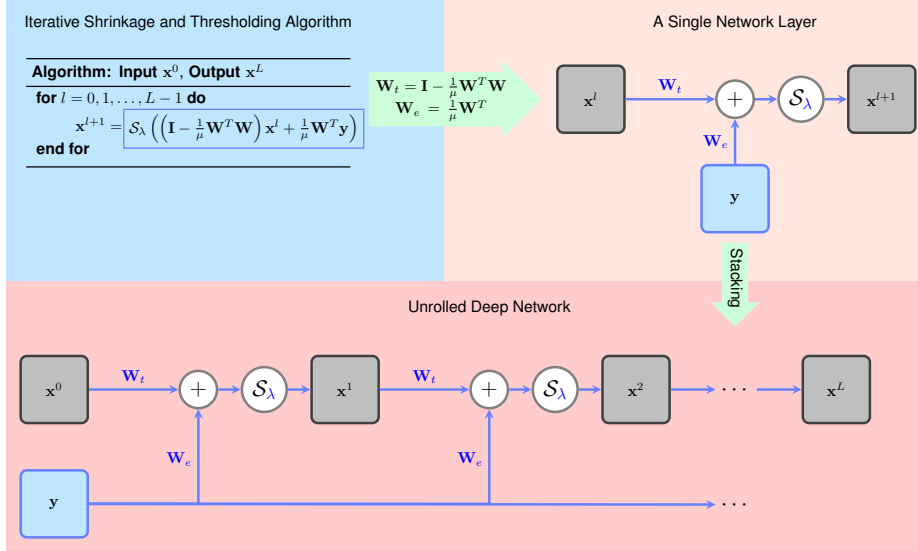


Figure 1.2 Illustration of LISTA: one iteration of ISTA executes a linear and then a non-linear operation and thus can be recast into a network layer; by stacking the layers a deep network is formed. The network is subsequently trained using paired inputs and outputs by back-propagation to optimize the parameters \mathbf{W}_e , \mathbf{W}_t and λ . The trainable parameters in the network are colored in blue.

where μ is a positive parameter controlling the step size, and \mathcal{H}_k is the hard-thresholding operator which zeros out all but the largest (in magnitude) k coefficients of the vector. Similar to LISTA, in (Xin et al. 2016) $\mathbf{W}_t = \mathbf{I} - \frac{1}{\mu} \mathbf{W}^T \mathbf{W}$ and $\mathbf{W}_e = \frac{1}{\mu} \mathbf{W}^T$ are used instead of \mathbf{W} itself, which reduces the iteration (1.8) into the following version:

$$\mathbf{x}^{l+1} = \mathcal{H}_k \{ \mathbf{W}_t \mathbf{x}^l + \mathbf{W}_e y \}, \quad l = 0, 1, \dots \quad (1.9)$$

The authors then prove that, a necessary condition for the iteration (1.9) to recover a feasible solution to (1.7) is that, the weight coupling scheme $\mathbf{W}_t = \mathbf{I} - \mathbf{W}_e \mathbf{W}$ is satisfied, for some \mathbf{W} introduced here as a free variable. Note that this formula is reminiscent of the implicit re-parameterization scheme: $\mathbf{W}_t = \frac{1}{\mu} \mathbf{W}^T \mathbf{W}$. Furthermore, under the weight coupling constraint, when \mathbf{W} and \mathbf{W}_e additionally obey technical conditions, the iteration (1.9) recovers the underlying solution at a linear rate. In particular, \mathbf{W} needs to satisfy certain Restricted-Isometry-Property (RIP) conditions. The authors also articulate the exact forms of \mathbf{W}_e in order to ensure linear convergence. Compared to classical IHT, the iteration (1.9) necessitates a much more relaxed requirement on the RIP condition, which implies that the unrolled network is capable of recovering sparse signals from dictionaries with relatively more coherent columns.

Chen *et al.* (Chen, Liu, Wang & Yin 2018) study the LISTA network with layer specific parameters $\{\mathbf{W}_t^l, \mathbf{W}_e^l, \lambda^l\}_{l \in \mathbb{N}}$, and prove that, if LISTA recovers

the underlying sparse solution and if the sequence $\mathbf{W}_t^1, \mathbf{W}_t^2, \dots$ is bounded, then a similar weight coupling scheme must be satisfied asymptotically:

$$\begin{aligned} \mathbf{W}_t^l - (\mathbf{I} - \mathbf{W}_e^l \mathbf{W}) &\rightarrow 0, \quad \text{as } l \rightarrow \infty, \\ \lambda^l &\rightarrow 0, \quad \text{as } l \rightarrow \infty. \end{aligned}$$

When LISTA adopts the weight coupling parametrization $\mathbf{W} = \mathbf{I} - \mathbf{W}_e^l \mathbf{W}$, and employs a dedicated support selection technique, the resulting network is called LISTA-CPSS, where ‘‘CP’’ stands for weight coupling and ‘‘SS’’ stands for support selection. Chen *et al.* prove that, if the underlying solution \mathbf{x}^* is sufficiently sparse and bounded, then the sequence $\{\mathbf{W}_e^l, \lambda^l\}_{l \in \mathbb{N}}$ can be chosen according to certain values such that LISTA-CPSS recovers \mathbf{x}^* at a linear rate. As a follow-up, Liu *et al.* (Liu, Chen, Wang & Yin 2019) introduce certain mutual coherence conditions and analytically characterize optimal network parameters based on those conditions. Similar to the networks with trained weights, networks adopting analytic weights converge at a linear rate, which implies that analytic weights can be as efficient as learned weights. In addition, analytic weights are of much lower dimensionality compared to trained weights. However, determining the analytic weights can be a nontrivial task as typically another optimization problem has to be solved.

1.2.4 Unrolling Generic Iterative Algorithms

Although the initial motivation of Gregor *et al.*’s work (Gregor & LeCun 2010) was to increase the efficiency of sparse coding techniques via training, the underlying principles could be easily generalized. More specifically, provided with a certain iterative algorithm, we can unroll it into a corresponding deep network, following the procedures depicted in Fig. 1.3. The first step is to identify the analytic operations per iteration, which we represent abstractly as an h function, and the associated parameters, which we denote collectively as θ^l . The next task is to generalize the functional form of h into a more generic version \hat{h} , and correspondingly expand the parameters θ^l into an enlarged version $\hat{\theta}^l$ if necessary. For instance, in LISTA the parameter \mathbf{W} is substituted with \mathbf{W}_t and \mathbf{W}_e through the formula $\mathbf{W}_t = \mathbf{I} - \frac{1}{\mu} \mathbf{W}^T \mathbf{W}$ and $\mathbf{W}_e = \frac{1}{\mu} \mathbf{W}^T$. After this procedure each iteration can be recast into a network layer in the same spirit as LISTA. By stacking the mapped layers together we obtain a deep network with undetermined parameters, and then obtain optimal parameters through end-to-end training using real world datasets.

The exact approach to generalize h and θ^l s towards \hat{h} and $\hat{\theta}^l$ s is largely case specific. An extreme scenario is to strictly follow the original functional forms and parameters, i.e., to take $\hat{h} = h$ and $\hat{\theta}^l = \theta^l, \forall l$. In this way, the trained network corresponds exactly to the original algorithm with finite truncation and optimal parameters. In addition to efficiency enhancement thanks to training (Gregor & LeCun 2010), the unrolled networks can aid with estimating structured parameters such as filters (Solomon, Eldar, Mutzafi & Segev 2019) or dictionaries (Wang,

Liu, Yang, Han & Huang 2015) which are hard to design either analytically or by handcrafting. Alternatively, some operations may be replaced with a stand alone deep neural network such as Convolutional Neural Network (CNN) or Recurrent Neural Network (RNN). For instance, in (Hauptmann et al. 2018) the authors replace a proximal gradient update step with a CNN. In addition, the parameters can be layer specific instead of being shared across different layers. For instance, in (Adler & Öktem 2018) the authors plug in a CNN in each iteration step (layer) and allow the network parameters to differ. As it is, networks with shared parameters generally resemble RNN, while those with layer specific parameters mimic CNN, especially when there are convolutional structures embedded in layer-wise operations. It is important to note that such custom modifications may potentially sacrifice certain conceptual merits such as invalidating convergence guarantees, introducing departures from the original iterative algorithms, or undermining the interpretability to some extent; nevertheless, they are practically beneficial and critical for performance improvement because the representation capacity of the network can be significantly extended.

In addition to performance and efficiency benefits, unrolled networks can potentially reduce the number of parameters and hence storage footprints. Conventional generic neural networks typically reuse essentially the same architectures across different domains and thus require a large amount of parameters to ensure their representation power. In contrast, unrolled networks generally deliver significantly fewer parameters, as they implicitly transfer problem structures (domain knowledge) from iterative algorithms to unrolled networks and their structures are more specifically tailored towards target applications. These benefits not only ensure higher efficiency, but also provide better generalizability especially under limited training schemes (Yang et al. 2018), as will be demonstrated through concrete examples in Section 1.3.

The unrolled network can share inter-layer parameters, thus resembling a RNN, or carry over layer-specific parameters. Although parameter sharing could further reduce parameters, the RNN-like architecture significantly increases the difficulty in training. In particular, it may suffer from gradient explosion and vanishing problems. On the other hand, using layer specific parameters may lead to deviation from the original iterative algorithm and may no longer inherit the convergence guarantees. However, the networks can have larger capacity and become easier to train.

Another important concern when designing unrolled networks is to determine the optimal number of layers, which corresponds to the number of iterations in the iterative algorithm. Most existing approaches generally treat it as a hyper-parameter and determine it through cross-validation. However, recent theoretical breakthroughs (some of them reviewed in Section 1.2.3) regarding convergence rate of the unrolled network can shed some light and guide future efforts.

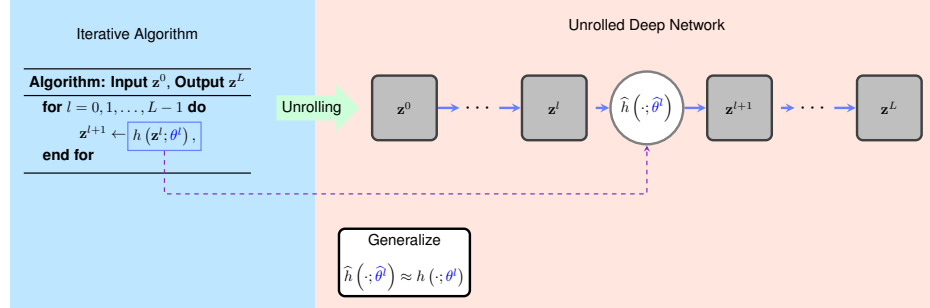


Figure 1.3 Illustration of the general idea of algorithm unrolling: given an iterative algorithm, we map one iteration (described as the function h parametrized by $\theta^l, l = 0, \dots, L - 1$) into a single network layer, and stack a finite number of layers to form a deep network. Feeding the data forward through an L -layer network is equivalent to executing the iteration L times (finite truncation). The parameters $\theta^l, l = 0, \dots, L - 1$ are learned from real datasets by training the network end-to-end to optimize the performance. They can either be shared across different layers or varying from layer to layer. The trainable parameters are colored in blue.

1.3 Deep Algorithm Unrolling for Biomedical Imaging

In recent years, algorithm unrolling has found wide applications in many areas of biomedical imaging. Traditionally, iterative algorithms have played a dominant role in solving various biomedical imaging problems. Recently, learning-based approaches, especially deep neural networks, have become increasingly popular. Algorithm unrolling bridges between well-grounded iterative algorithms and contemporary deep networks and has attracted growing research attention. In this section, we discuss how algorithm unrolling can be successfully applied towards biomedical image synthesis via several concrete cases.

1.3.1 Applications of Unrolling in Computed Tomography

In general, Computed Tomography (CT) refers to a class of imaging techniques that reconstruct the original signal out of its directional projections (slices). For instance, in X-ray CT, a mobilized X-ray source rotates around the patient to emit narrow beams of X-rays, which are then received by X-ray detectors located opposite of the X-ray source. The X-rays pass through the patient to create image slices. In its simplest form, this procedure can be described by the well-known Radon transform. In 2D, the Radon transform is given by the following formula:

$$p(\xi, \phi) = \int f(x, y) \delta(x \cos(\phi) + y \sin(\phi) - \xi) dx dy,$$

where f is the imaged signal and δ is the Dirac delta function. The function p is often referred to as a *sinogram*. To invert the Radon transform, the classical central slice theorem plays a critical role as it relates the Fourier transform of the

original signal and its sinogram. This relationship gives rise to the Filtered Back Projection (FBP) algorithm: the sinogram is first filtered by a so-called ramp filter, and then back-projected to obtain the original signal. Practical challenges of CT include short scanning time, low-dose, motion and noise.

In an early work that employs deep CNN for CT (Jin, McCann, Froustey & Unser 2017), the authors observe the architectural similarity between the popular U-net (Ronneberger, Fischer & Brox 2015) and the unrolled ISTA network. They then combine FBP with U-net to construct a deep network called FBPCNN. Through extensive experimental studies on sparse-view X-ray CT reconstruction, FBPCNN offers clear benefits over traditional iterative reconstruction techniques such as the Total-Variation (TV) regularization approach. In particular, FBPCNN achieves over 3dB Signal-to-Noise Ratio (SNR) improvement over TV on a biomedical dataset that comprises 500 real in-vivo CT images, and reduces the running time from several minutes to less than a second. Compared with conventional deep networks such as residual networks, FBPCNN also achieves more than 1dB higher SNR on the same dataset.

An emerging CT technique is Photo Acoustic Tomography (PAT) that provides high resolution 3D images by sensing laser-generated ultrasound. In (Hauptmann et al. 2018) the authors develop a deep learning technique to reconstruct high-resolution 3D images from restricted photo acoustic measurements. Modeling the acoustic signal via the wave equation, the initial pressure \mathbf{x} and the measured photo acoustic signal \mathbf{y} satisfy a linear mapping

$$\mathbf{y} = \mathbf{W}\mathbf{x},$$

and thus PAT can be carried out by solving a linear inverse problem. A typical approach is to solve the following regularized problem:

$$\min_{\mathbf{x}} \rho(\mathbf{y}, \mathbf{W}\mathbf{x}) + \lambda\mathcal{R}(\mathbf{x}), \quad (1.10)$$

where $\rho(\cdot, \cdot)$ is a metric measuring the data consistency, \mathcal{R} is a regularizer and λ is the regularization coefficient. A simple approach to solving (1.10) is the Proximal Gradient Descent (PGD) algorithm, which performs the following iterations:

$$\mathbf{x}_{k+1} \leftarrow \text{prox}_{\mathcal{R}}(\mathbf{x}_k - \gamma_{k+1}\nabla\rho(\mathbf{y}, \mathbf{W}\mathbf{x}_k); \lambda\gamma_{k+1}), \quad (1.11)$$

where $\gamma_{k+1} > 0$ controls the step size. Hauptmann *et al.* replace the proximal operator with a CNN and learn the arithmetic operations (subtraction, multiplication) rather than fixing it according to the gradient descent rule (1.11). In other words, they propose to unroll the following update procedures:

$$\mathbf{x}_{k+1} = G_{\theta_k}(\nabla\rho(\mathbf{y}, \mathbf{W}\mathbf{x}_k), \mathbf{x}_k),$$

where G denotes a CNN and θ_k are its parameters. The corresponding unrolled network is depicted visually in Fig. 1.4. The network is dubbed Deep Gradient Descent (DGD). To train the network, a stage-wise scheme is employed: at the k -th stage, θ_k is optimized by minimizing the Mean-Square-Error (MSE) loss

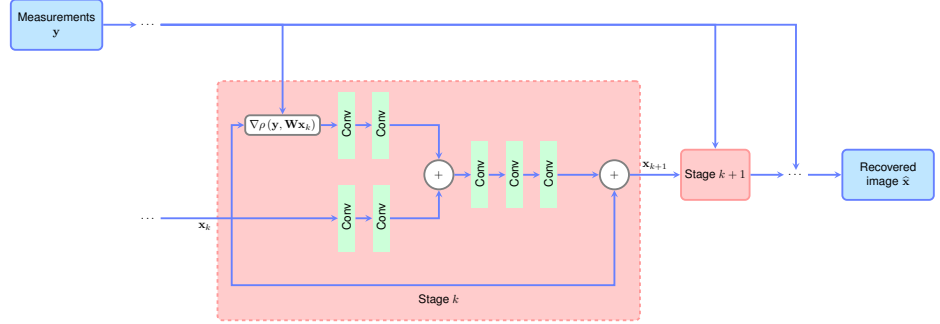


Figure 1.4 Representation of DGD (Hauptmann et al. 2018): each stage comprises a gradient descent iteration with the proximal operator replaced by a CNN. The CNN takes as input a concatenation of \mathbf{x}_k and the gradient $\nabla\rho(\mathbf{y}, \mathbf{W}\mathbf{x}_k)$. It also adopts a skip connection from \mathbf{x}_k to \mathbf{x}_{k+1} , which implies it learns a residual mapping.

between \mathbf{x}_k and groundtruth \mathbf{x}^* while holding other $\theta_j (j \neq k)$'s fixed. Experimentally, DGD achieves nearly 1dB improvement in Peak Signal-to-Noise Ratio (PSNR) over U-Net and more than 3dB over TV reconstruction on an in-vivo dataset of a human palm. Furthermore, compared with conventional deep networks such as U-Net, DGD proves its superior robustness against perturbations of measurement procedures or targets, by showing only slight deterioration in reconstruction quality under small perturbations such as varying sub-sampling patterns, noise levels, or deviations in sound speed.

In a closely related technique (Gupta, Jin, Nguyen, McCann & Unser 2018), Gupta *et al.* unroll the PGD algorithm, and similarly replace the proximal operator with a CNN. However, they do not learn the arithmetic operations and instead follow the update rule in (1.11). In addition, they introduce a relaxation to the PGD update, in order to maintain its convergence guarantee even when the proximal operator is substituted with a CNN. The unrolled network, dubbed Relaxed Projected Gradient Descent (RPGD), yields substantially improved CT recovery, as depicted in Fig. 1.5.

Low-dose X-ray CT is an intriguing technique as X-ray CT causes potential cancer risks due to radiation exposure. A drawback of this approach, however, is the low SNR of the projections due to noise, and thus power imaging techniques are required to retrieve high-quality reconstructed images. To overcome the challenge of noisy measurements, Kang *et al.* (Kang, Chang, Yoo & Ye 2018) build a Wavelet Residual Network (WavResNet) based on a theory of deep convolutional framelet for deep learning-based denoising. Suppose we seek to estimate a ground-truth signal $\mathbf{x}^* \in \mathbb{R}^n$ from its noisy measurement $\mathbf{y} \in \mathbb{R}^n$:

$$\mathbf{y} = \mathbf{x}^* + \mathbf{n},$$

where $\mathbf{n} \in \mathbb{R}^n$. A traditional approach is frame-based denoising, which shrinks

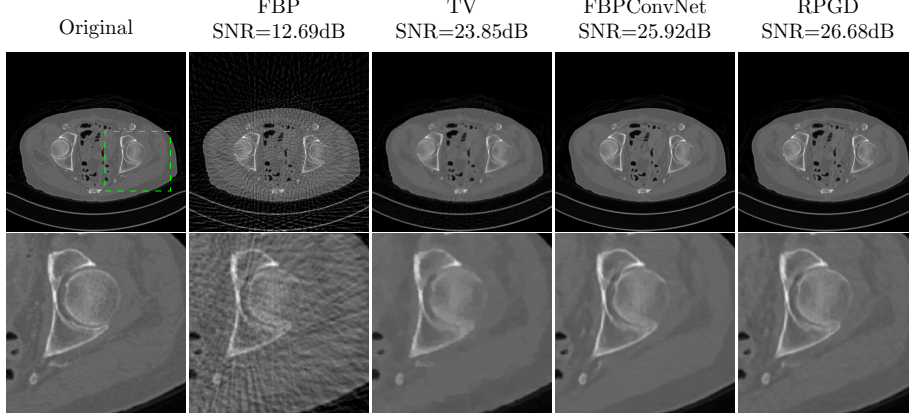


Figure 1.5 Experimental comparisons between RPGD (Gupta et al. 2018) and state-of-the-art reconstruction algorithms (including FBPConvNet from (Jin et al. 2017)) over a test sample from noiseless measurements with 45 views (x16 dosage reduction). The SNR values are also included for quantitative comparisons. The first row shows the full images and the second row shows their magnified portions, respectively. Images are courtesy of Michael Unser at EPFL (Gupta et al. 2018).

the frame coefficient α of the signal by solving:

$$\min_{\mathbf{x}, \alpha} \frac{\mu}{2} \|\mathbf{y} - \mathbf{x}\|_2^2 + \frac{1-\mu}{2} \{ \|\mathbf{W}\mathbf{x} - \alpha\|_2^2 + \lambda \|\alpha\|_1 \},$$

where $\lambda, \mu > 0$ are the regularization coefficients and \mathbf{W} is the analysis operator of the frame. The corresponding proximal update equation is given by:

$$\mathbf{x}_{k+1} = \mu\mathbf{y} + (1-\mu)\mathbf{W}^T \mathcal{S}_\lambda(\mathbf{W}\mathbf{x}_k), \quad (1.12)$$

where \mathcal{S}_λ is the soft-thresholding operator with thresholding value λ (Li, Fan, Ji & Shen 2014, Dong, Jiang & Shen 2017).

Kang *et al.* (Kang et al. 2018) claim that the term $\mathbf{W}^T \mathcal{S}_\lambda(\mathbf{W}\mathbf{x}_k)$ can be regarded as a CNN based on the deep convolutional framelet theory (Ye, Han & Cha 2018). In short, the analysis and synthesis operators of a frame can be concatenated to form an encoder-decoder layer structure which corresponds to a CNN, and the shrinkage operation can be implicitly obtained by reducing the channels in the CNN. The update rule (1.12) is then substituted with

$$\mathbf{x}_{k+1} = \mu\mathbf{y} + (1-\mu)\mathcal{Q}(\mathbf{x}_k; \phi, \tilde{\phi}) \quad (1.13)$$

where \mathcal{Q} is the CNN corresponding to the framelet, with undetermined filter coefficients $\phi, \tilde{\phi}$ corresponding to the primal and dual frames, respectively. The unrolled networks are formed out of the update rules (1.13) and the unknown parameters are learned; the parameters are shared across different iterations giving rise to a RNN-like architecture. In addition, Kang *et al.* (Kang et al. 2018) slightly modify the update rules (1.13) to ensure convergence. Through extensive

experimental results, WavResNet shows its advantage at noise reduction and preserving texture details of the organ while maintaining the lesion information over state-of-the-art techniques.

A related technique that also focuses on low-dose CT reconstruction is the work by Adler *et al.* (Adler & Öktem 2018), where the Proximal-Dual Hybrid Gradient (PDHG) algorithm is generalized and unrolled into a learnable network. Technically, the PDHG algorithm solves problems of the following form:

$$\min_{\mathbf{x}} \mathcal{P}(\mathcal{K}(\mathbf{x})) + \mathcal{D}(f), \quad (1.14)$$

where \mathcal{K} is an operator over signal \mathbf{x} and \mathcal{P}, \mathcal{D} are functionals on the primal and dual spaces, respectively. Problem (1.14) has many interesting instances; in particular, the TV-regularized CT can be instantiated by letting $\mathcal{K}(\mathbf{x}) := [\mathcal{R}(\mathbf{x}), \nabla \mathbf{x}]$, $\mathcal{P}([\mathbf{h}_1, \mathbf{h}_2]) := \|\mathbf{h}_1 - \mathbf{y}\|_2^2 + \|\mathbf{h}_2\|_1$ and $\mathcal{D} := 0$, which gives rise to the following optimization problem:

$$\min_{\mathbf{x}} \|\mathcal{R}(\mathbf{x}) - \mathbf{y}\|_2^2 + \lambda \|\nabla \mathbf{x}\|_1,$$

where \mathcal{R} is the Radon transform operator, ∇ is the gradient operator, and $\lambda > 0$ is a regularization coefficient. The PDHG algorithm essentially performs the following iterations for $k = 1, 2, \dots$:

$$\begin{aligned} \mathbf{z}_{k+1} &\leftarrow \text{prox}_{\mathcal{P}^*}(\mathbf{z}_k + \sigma \mathcal{K}(\bar{\mathbf{x}}_k); \sigma), \\ \mathbf{x}_{k+1} &\leftarrow \text{prox}_{\mathcal{D}}(\mathbf{x}_k - \tau [\partial \mathcal{K}(\mathbf{x}_k)]^*(\mathbf{z}_{k+1}); \tau), \\ \bar{\mathbf{x}}_{k+1} &\leftarrow \mathbf{x}_{k+1} + \gamma(\mathbf{x}_{k+1} - \mathbf{x}_k), \end{aligned}$$

where $*$ is the Fenchel conjugate and ∂ is the Fréchet derivative. For definitions of these terms, see (Rockafellar 1970). The operator $\text{prox}_{\mathcal{F}}(\cdot; \lambda)$ is the proximal operator over functional \mathcal{F} and parameter λ , given by

$$\text{prox}_{\mathcal{F}}(\mathbf{x}; \lambda) = \arg \min_{\mathbf{x}'} \mathcal{F}(\mathbf{x}') + \frac{1}{2\lambda} \|\mathbf{x}' - \mathbf{x}\|_2^2.$$

In a similar spirit to (Hauptmann *et al.* 2018), Adler *et al.* generalize the update rules by replacing the proximal operators with CNNs, and substituting the arithmetic operations (summation, multiplication, etc) as learnable operations, giving rise to the following iterations:

$$\begin{aligned} \mathbf{z}_k &\leftarrow \Gamma_{\theta_k^d}(\mathbf{z}_{k-1}, \mathcal{K}(\mathbf{x}_{k-1}^{(2)}), \mathbf{y}), \\ \mathbf{x}_k &\leftarrow \Lambda_{\theta_k^p}(\mathbf{x}_{k-1}, [\partial \mathcal{K}(\mathbf{x}_{k-1}^{(1)})]^*(\mathbf{z}_k^{(1)})), \end{aligned}$$

where $\Lambda_{\theta_k^p}$ and $\Gamma_{\theta_k^d}$ are CNNs replacing primal and dual operators, with parameters θ_k^p and θ_k^d , respectively. The notation $\mathbf{x}^{(1)}$ and $\mathbf{x}^{(2)}$ selects first and second blocks of coefficients in \mathbf{x} to permit “memory” across iterations. A deep network, dubbed Learned Primal-Dual, can then be formed by stacking iterations (layers) together. The parameters θ_k^p and θ_k^d are learned by minimizing the MSE loss.

Compared with FBP, TV reconstruction and conventional deep networks such

as U-Net, Learned Primal-Dual obtains more than 6dB improved PSNR for the Shepp-Logan phantom, and over 2dB improvement on human phantoms on average. In terms of Structural Similarity Index (SSIM), it also outperforms its competitors by a large margin. The runtime is on the same order as FBP, rendering it amenable to time-critical applications.

Another technique for low-dose CT reconstruction is the BCD-Net (Chun & Fessler 2018, Chun, Zheng, Long & Fessler 2019), where the authors generalize the block coordinate descent algorithm for model-based inversion, by integrating a CNN as a learnable denoiser. As a follow-up of the learned primal-dual network, Wu (Wu, Kim, Dong, Fakhri & Li 2018) concatenates it with a detection network, and applies joint fine-tuning after training both networks individually. Their jointly fine-tuned network achieves comparable performance with the detector trained on the fully-sampled data and outperforms detectors trained on the reconstructed images.

1.3.2 Unrolling in Super-resolution Microscopy

Optical microscopy generates magnified images of small objects by using visible light and a system of lenses, thus enabling different research fields like cell biology and microbiology. However, the spatial resolution is limited by the physics of light, which thereby poses a hard limit on resolution. The diffraction of light makes structures too blurry to be resolved once they are smaller than approximately half the wavelength of light (Huang 2010, Solomon et al. 2019). This limitation is circumvented using photo-activated fluorescent molecules. In 2-D Single Molecule Localization Microscopy (SMLM), a sequence of diffraction-limited images, produced by a sparse set of emitting fluorophores with minimally overlapping Point Spread Functions (PSFs) is acquired, allowing the emitters to be localized with high precision (Dardikman-Yoffe & Eldar 2020). However, the need for low emitter-density results in poor temporal resolution.

In (Dardikman-Yoffe & Eldar 2020), the authors unroll the SPARSity based super-resolution COrrrelation Microscopy (SPARCOM) (Solomon et al. 2019) method to incorporate domain knowledge, resulting in Learned SPARCOM (LSPARCOM). Specifically, LSPARCOM aims to recover a single $M \times M$ high resolution image \mathbf{X} , corresponding to the locations of the emitters on a fine grid, from a set of T low-resolution frames of size $N \times N$ with $N < M$. A single frame taken at time t is denoted as $\mathbf{Y}(t)$. The method exploits the sparse nature of the fluorophores distribution, alongside a statistical prior of uncorrelated emissions. The sparsity assumption implies that the overall number of emitter-containing-pixels is significantly smaller than the total number of pixels in the high resolution grid, yet, as opposed to classical methods for SMLM, it accounts for scenarios with overlapping PSFs formed by adjacent emitters.

The authors formulate a sparse recovery problem on the temporal variance image given by:

$$\mathbf{g}_Y = \mathbf{W}\mathbf{x}, \quad (1.15)$$

where $\mathbf{g}_Y \in \mathbb{R}^{N^2}$ comprises temporal variances of the set of T low-resolution frames, \mathbf{W} is a dictionary matrix based on the PSF, and \mathbf{x} comprises variances of the emitter fluctuation on a high-resolution grid. The unknown \mathbf{x} can be determined by solving a sparsity constrained optimization problem similar to (1.3) with an additional non-negativity constraint over \mathbf{x} , which in turn can be solved via the ISTA algorithm presented in Section 1.2.1. The algorithm can be further unrolled into a network whose architecture resembles LISTA. Different from LISTA, the authors propose the following proximal operator instead of the soft-thresholding operator defined in (1.5):

$$\mathcal{S}_{\alpha,\beta}^+(x) \triangleq \frac{\max\{0, x\}}{1 + \exp[-\beta(|x| - \alpha)]}, \quad (1.16)$$

where α and β are hyper-parameters. When applied to vectors and matrices, $\mathcal{S}_{\alpha,\beta}^+(\cdot)$ operates element-wise. This is a sigmoid-based approximation of the positive hard thresholding operator, which is the proximal operator for the ℓ^0 norm, that accounts for increased sparsity. Furthermore, it performs one-sided thresholding due to the non-negativity constraint.

For training, the authors introduce a compatible loss function given by:

$$Loss = \frac{1}{M^2} \sum_{i,j=1}^M \mathbf{B}(i,j) |\hat{\mathbf{X}}(i,j) - \mathbf{X}^*(i,j)|^2 + \lambda [1 - \mathbf{B}(i,j)] |\hat{\mathbf{X}}(i,j)|, \quad (1.17)$$

where $\hat{\mathbf{X}}$ is the output of the network, \mathbf{X}^* is the ground truth image, and \mathbf{B} is a binary mask, created by binarizing \mathbf{X}^* , which eliminates entries that do not contain emitters. This encourages the network to output signals coming only from emitters while suppressing the background.

Experimental results across different test sets show that the unrolled network can obtain super-resolution images from a small number of high emitter density frames without knowledge of the optical system. All the methods that are compared were evaluated on the quality of the reconstruction based on the exact same input frames, while the input for LSPARCOM is a single image, which is constructed by calculating the temporal variance of all the high density frames. Fig. 1.6 provides an example for performance evaluation of SPARCOM, LSPARCOM, and Deep-STORM (Nehme, Weiss, Michaeli & Shechtman 2018). Deep-STORM is another learning based method, devised for the problem at hand. Two examples are brought for each method, one that incorporates prior knowledge (Deep-STORM net2 and LSPARCOM TU which were trained for similar imaging parameters as in the test set and SPARCOM with known PSF), and the second without prior knowledge. While all three methods achieve good results when incorporating prior knowledge, LSPARCOM is superior when generalizing to new data. Quantitatively speaking, SPARCOM reconstruction took 39.32 sec, LSPARCOM reconstruction took 10.8 sec, and Deep-STORM took 280.38 sec for 500 128×128 input frames. Moreover, LSPARCOM is highly parameter efficient: 9058 parameters in 10 folds of LSPARCOM vs. 1.3M trainable parameters

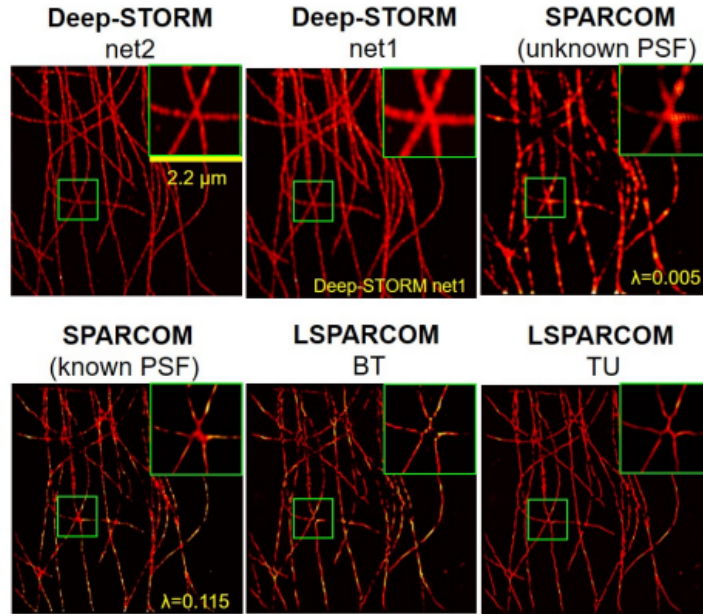


Figure 1.6 Performance evaluation for experimental tubulin sequence, composed of 500 high-density frames [35]. A difficult area for reconstruction is shown magnified in the green box. From top left to bottom right: reconstructions using Deep-STORM architecture trained on different datasets (net1 and net 2), SPARCOM reconstruction with unknown PSF, SPARCOM reconstruction using explicit knowledge of the PSF, reconstructions using LSPARCOM architecture trained on different datasets (BT, TU). Figure reproduced from (Dardikman-Yoffe & Eldar 2020) with authors' permission.

in Deep-STORM. Consequently, the network achieves runtime savings compared to other learning-based methods.

1.3.3 Applications of Unrolling in Ultrasound

An important ultrasound-based modality is Contrast Enhanced UltraSound (CEUS) (Furlow 2009), which allows the detection and visualization of small blood vessels. The main idea behind CEUS is the use of encapsulated gas microbubbles, serving as Ultrasound Contrast Agents (UCAs). UCAs are injected intravenously and can flow throughout the vascular system due to their small size. To visualize them, strong clutter signals originating from stationary or slowly moving tissues must be removed, as they introduce significant artifacts in the resulting images. The latter poses a major challenge in ultrasonic vascular imaging (Van Sloun, Cohen & Eldar 2019).

In (Solomon et al. 2020), the authors suggest a method for clutter suppression by applying the well-known low-rank and sparse matrix decomposition technique,

a.k.a Robust Principal Component Analysis (RPCA), and unrolling the corresponding algorithm into a deep network named Convolutional rObust pRincipal cOmpoNent Analysis (CORONA). Specifically, they model the acquired contrast enhanced ultrasound signal as a combination of a low-rank matrix (tissue) and a sparse outlier signal (UCAs).

In UltraSound (US) imaging, a series of pulses are transmitted to the imaged medium. The resulting echoes from the medium are received in each transducer element and then combined in a process called beamforming to produce a focused image. If we denote the vertical and axial coordinates as x , z , and the frame number as t , the observed signal from a specific point in time-space, denoted as $Y(x, z, t)$, can be described as the sum of echoes returned from the blood and CEUS signal $S(x, z, t)$ as well as from the tissue $L(x, z, t)$, contaminated by additive noise $N(x, z, t)$. When acquiring a series of movie frames $t = 1, \dots, T$, and stacking them as columns in a matrix \mathbf{Y} , the relation between the measurements and the signal scan be described via:

$$\mathbf{Y} = \mathbf{H}_1 \mathbf{L} + \mathbf{H}_2 \mathbf{S} + \mathbf{N}, \quad (1.18)$$

where \mathbf{H}_1 and \mathbf{H}_2 are measurement matrices of appropriate dimensions. Similar to \mathbf{Y} , \mathbf{L} and \mathbf{S} are matrices whose columns contain per-frame data. The tissue matrix \mathbf{L} can be described as a low-rank matrix, due to its high spatio-temporal coherence. The CEUS echoes matrix \mathbf{S} is assumed to be sparse, as blood vessels typically sparsely populate the imaged medium. Under the assumptions on the matrices \mathbf{L} and \mathbf{S} , their recovery can be obtained by solving the following convex optimization problem:

$$\min_{\mathbf{L}, \mathbf{S}} \frac{1}{2} \|\mathbf{Y} - (\mathbf{H}_1 \mathbf{L} + \mathbf{H}_2 \mathbf{S})\|_F^2 + \lambda_1 \|\mathbf{L}\|_* + \lambda_2 \|\mathbf{S}\|_{1,2}, \quad (1.19)$$

where $\|\cdot\|_*$ stands for the nuclear norm (i.e., the sum of the singular values of \mathbf{L}), $\|\cdot\|_{1,2}$ stands for the mixed $\ell^{1,2}$ norm (i.e., the sum of the ℓ^2 norms of each row of \mathbf{S}), and λ_1 and λ_2 are regularization coefficients promoting low rank structure of \mathbf{L} and sparsity of \mathbf{S} , respectively.

Problem (1.19) can be solved using a generalized version of ISTA over matrices, by utilizing the proximal mapping corresponding to the nuclear norm and mixed $\ell_{1,2}$ norm (Monga et al. 2019). In each iteration l , the estimations for both \mathbf{S} and \mathbf{L} are updated as follows:

$$\begin{aligned} \mathbf{L}^{l+1} &= \mathcal{T}_{\frac{\lambda_1}{\mu}} \left\{ \left(\mathbf{I} - \frac{1}{\mu} \mathbf{H}_1^H \mathbf{H}_1 \right) \mathbf{L}^l - \mathbf{H}_1^H \mathbf{H}_2 \mathbf{S}^l + \mathbf{H}_1^H \mathbf{Y} \right\}, \\ \mathbf{S}^{l+1} &= \mathcal{S}_{\frac{\lambda_2}{\mu}}^{1,2} \left\{ \left(\mathbf{I} - \frac{1}{\mu} \mathbf{H}_2^H \mathbf{H}_2 \right) \mathbf{S}^l - \mathbf{H}_2^H \mathbf{H}_1 \mathbf{L}^l + \mathbf{H}_2^H \mathbf{Y} \right\}. \end{aligned} \quad (1.20)$$

Here $\mathcal{T}_\lambda\{\mathbf{X}\}$ is the singular value thresholding operator that performs soft thresholding over the singular values of \mathbf{X} with threshold λ , $\mathcal{S}_\lambda^{1,2}$ performs row-wise soft thresholding with parameter λ , and μ is the step size parameter for ISTA.

To construct the unrolled network, Solomon *et al.* replace matrix multiplications with convolutional layers that are subsequently fed into the non-linear proximal mappings. The l -th iteration then becomes:

$$\begin{aligned}\mathbf{L}^{l+1} &= \mathcal{T}_{\lambda_1^l} \{ \mathbf{W}_5^l * \mathbf{L}^l + \mathbf{W}_3^l * \mathbf{S}^l + \mathbf{W}_1^l * \mathbf{Y} \}, \\ \mathbf{S}^{l+1} &= \mathcal{S}_{\lambda_2^l}^{1,2} \{ \mathbf{W}_6^l * \mathbf{S}^l + \mathbf{W}_4^l * \mathbf{L}^l + \mathbf{W}_2^l * \mathbf{Y} \},\end{aligned}\tag{1.21}$$

where $\mathbf{W}_i^l, i = 1, \dots, 6$ are a series of convolution filters that are learned from the data in the l -th layer, $*$ acts on both spatial and temporal dimensions and performs multi-channel convolution, and λ_1^l, λ_2^l are thresholding parameters for the l -th layer. The architecture is illustrated in Fig. 1.7, in which \mathbf{L}^0 and \mathbf{S}^0 are set to some initial guess, and the output after L iterations, denoted \mathbf{S}^L , is used as the estimate of the desired sparse matrix \mathbf{S} .

The network is trained using back-propagation in a supervised manner. Training examples consists of observed matrices along with their corresponding ground truth \mathbf{L}^* and \mathbf{S}^* matrices (refer to (Solomon et al. 2020) for more details on how the dataset is generated). The loss function is chosen as the sum of the MSE between \mathbf{L}^* and \mathbf{S}^* to the values predicted by the network.

Compared with state-of-the-art approaches, CORONA demonstrates vastly improved reconstruction quality and has much fewer parameters. Fig. 1.8 provides visual results, demonstrating the power of CORONA to properly separate the low rank matrix and the sparse matrix. Fig. 1.8a shows the temporal maximum intensity projection (MIP) image of the input movie (50 frames). It can be seen that the UCA signal, depicted as randomly twisting lines, is masked considerably by the simulated tissue signal. Fig. 1.8b and Fig. 1.8d illustrate the ground truth MIP images of the UCA signal and tissue signal respectively, whereas Fig. 1.8c and Fig. 1.8e presents the MIP images of the recovered UCA signal and tissue signal via CORONA.

Another approach that leverages deep algorithm unrolling is used for super resolution US (Van Sloun et al. 2019, Bar-Shira, Grubstein, Rapson, Suhani, Atar, Peri-Hanania, Rosen & Eldar 2021), where UCAs are pinpointed and tracked through a sequence of US frames, to yield super-resolution images of the microvasculature, thus circumventing the diffraction limited resolution of conventional ultrasound. Unrolling is used to derive a robust method for super resolution US that is suited to various imaging conditions and does not depend on prior knowledge such as the PSF of the system.

By leveraging the signal structure, i.e., assuming that the UCAs distribution is sparse on a sufficiently high-resolution grid, and assuming that the US frames contain only UCAs signals (i.e., at absence of tissue clutter and noise), the model has the same form as (1.2), where \mathbf{x} is a vector that describes the sparse microbubble distribution on a high-resolution image grid, \mathbf{y} is the vectorized image frame of the ultrasound sequence, \mathbf{W} is a dictionary matrix derived from the PSF of the system, and \mathbf{n} is a noise vector. Again ISTA can be employed to solve this problem.

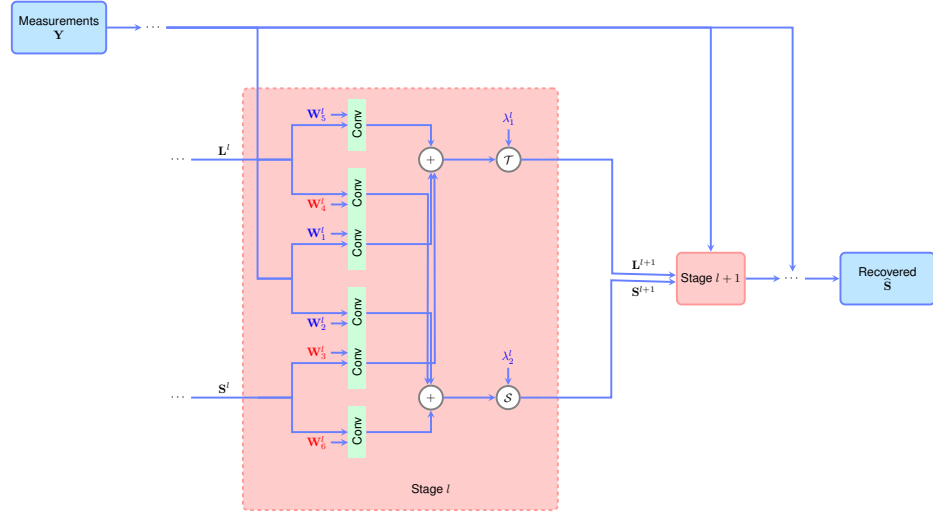


Figure 1.7 Diagram representation of CORONA. Trainable parameters are colored in blue. The learned network draws its architecture from the iterative algorithm. Here \mathbf{Y} is the input measurement matrix, and \mathbf{S}^l and \mathbf{L}^l are the estimated sparse and low-rank matrices in each layer, respectively.

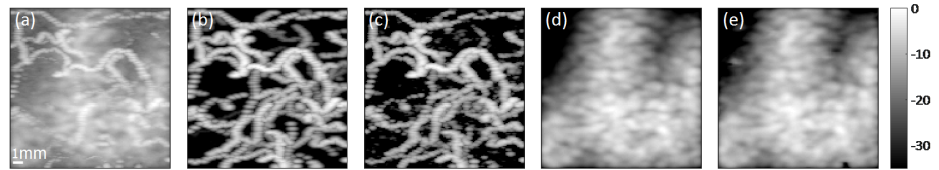


Figure 1.8 Sample experimental results demonstrating recovery of Ultrasound Contrast Agents (UCAs) from cluttered Maximum Intensity Projection (MIP) images. (a) MIP image of the input movie, composed from 50 frames of simulated UCAs cluttered by tissue. (b) Ground-truth UCA MIP image. (c) Recovered UCA MIP image via CORONA. (d) Ground-truth tissue MIP image. (e) Recovered tissue MIP image via CORONA. Color bar is in dB. Figure reproduced from (Solomon et al. 2020) with authors' permission.

The unrolled network, named deep unrolled ultrasound localization microscopy (ULM), is similar to LISTA, only that the soft-thresholding operator is substituted with a sigmoid-based soft-thresholding operation to avoid vanishing gradients during training (Zhang 2001). The network is trained using back-propagation under supervision of synthetically generated 2D images of point sources.

The authors trained a ten-layer deep network comprising 5×5 convolutional kernels. Fig. 1.9 provides visual results of deep unrolled ULM for super-resolution vascular imaging of a rat's spinal cord exhibiting a smooth reconstruction of the vasculature. Compared with an encoder–decoder approach devised for the same

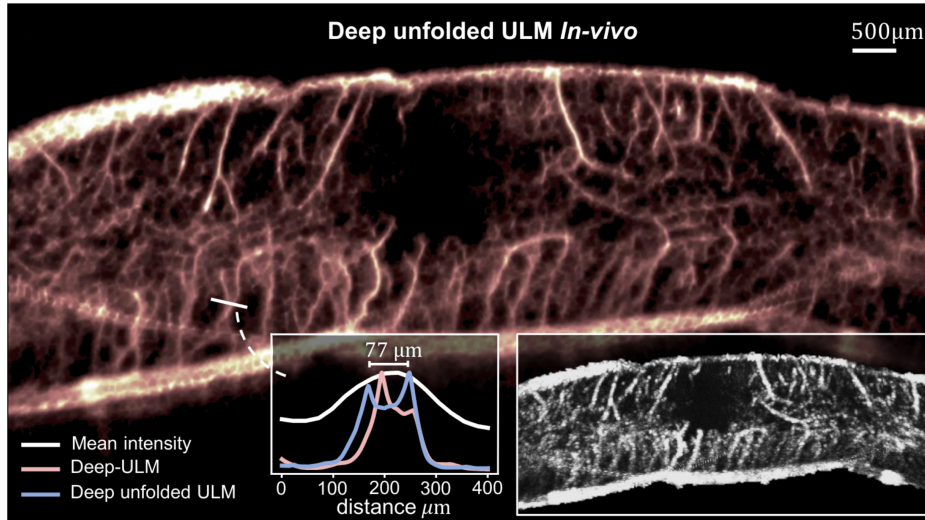


Figure 1.9 Deep unrolled ULM for super-resolution vascular imaging of a rat's spinal cord. Right rectangle: standard maximum intensity projection across a sequence of frames. Left rectangle: spatial resolution comparison between the deep unrolled ULM, and Deep-ULM. Figure reproduced from (Van Sloun et al. 2019) with authors' permission.

task and trained on the same data, named deep-ULM as proposed in (Van Sloun et al. 2019), deep unrolled ULM exhibited a drastically lower memory footprint and reduced power consumption, in addition to achieving higher inference rates and improved generalization when encountering new data. This can be seen in the spatial resolution comparison in Fig. 1.9, showing the superior capability of deep unrolled ULM to separate close structures. Recently, the method was harnessed to improve breast lesion characterization (Bar-Shira et al. 2021). Recoveries of three in vivo human scans of lesions in breasts of three patients were shown. Fig. 1.10 presents the recoveries of the three lesions along with the B-Mode US images that are used in clinical practice. The results reveal vascular structures that are not seen in the B-Mode images. Furthermore, the recoveries show unique vascular structure for each lesion, thus assisting the differentiation between the lesions.

1.3.4 Applications of Unrolling in Medical Resonance Imaging

A typical Magnetic Resonance Imaging (MRI) system comprises the following components: a primary magnet which exerts a primary magnetic field, gradient magnets which create spatial variation of the magnetic field and allow spatial encoding of the signal, Radio-Frequency (RF) coils which send out and receive a series of RF pulses and magnetic field gradients, and a computer system which decodes the received signal and reconstructs the original image of interest. For-

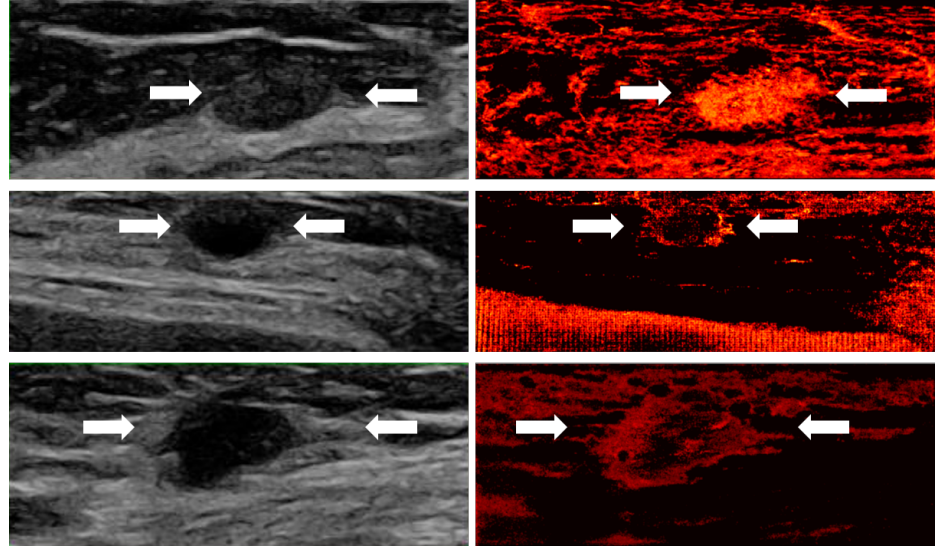


Figure 1.10 Super resolution demonstrations in human scans of three lesions in breasts of three patients. Left: B-mode images. Right: super resolution recoveries. The white arrows point at the lesions; Top: fibroadenoma (benign). The super resolution recovery shows an oval, well circumscribed mass with homogeneous high vascularization. Middle: cyst (benign). The super resolution recovery shows a round structure with high concentration of blood vessels at the periphery of the lesion. Bottom: invasive ductal carcinoma (malignant). The super resolution recovery shows an irregular mass with ill-defined margins, high concentration of blood vessels at the periphery of the mass, and a low concentration of blood vessels at the center of the mass. Figure reproduced from (Bar-Shira et al. 2021) with authors' permission.

mally speaking, the signal $\mathbf{y}(t)$ received in the receiver at time t is given by

$$\mathbf{y}(\mathbf{k}, t) = \int \mathbf{x}(x, y, z) \exp\{-j2\pi(k_x x + k_y y + k_z z)\} dx dy dz,$$

where \mathbf{x} is the image, x, y, z is the spatial location, and $\mathbf{k} = (k_x, k_y, k_z)$ is the k -space location at time t . In practice, a discretized model is commonly used:

$$\mathbf{y}(\mathbf{k}_i) = \sum_l \mathbf{x}(\mathbf{r}_l) \exp\{-j2\pi \mathbf{k}_i \cdot \mathbf{r}_l\},$$

where \mathbf{k}_i and \mathbf{r}_l are k -space and spatial locations and \cdot denotes the dot product between 3D vectors. That is, the measured signal \mathbf{y} comprises a series of Fourier encoding of the signal \mathbf{x} . In compressed MRI, only a subset of Fourier samples are observed, which gives rise to the following linear compressive imaging model:

$$\mathbf{y} = \mathbf{S}\mathbf{F}\mathbf{x},$$

where $\mathbf{F} \in \mathbb{C}^{m \times m}$ is the Fourier matrix and $\mathbf{S} \in \{0, 1\}^{n \times m}$ is the subsampling matrix. In the MRI literature, more advanced imaging models are developed to account for other factors such as inhomogeneity of the magnetic fields, coupling

between gradient coils, timing inaccuracies and motion. For a thorough review of these models, see (Doneva 2020).

To accelerate data acquisition of dynamic MRI, Qin *et al.* (Qin, Schlemper, Caballero, Price, Hajnal & Rueckert 2018) propose a Convolutional Recurrent Neural Network (CRNN) that captures temporal dependencies and reconstructs high quality cardiac MR images from highly undersampled k -space data. They first analyze the following classical regularized inverse problems:

$$\min_{\mathbf{x}} \mathcal{R}(\mathbf{x}) + \lambda \|\mathbf{y} - \mathbf{S}\mathbf{F}\mathbf{x}\|_2^2, \quad (1.22)$$

where \mathbf{x} comprises a sequence of complex-valued MR images, \mathcal{R} is the regularization functional and λ is the (reciprocal) regularization coefficient. By introducing an extra variable \mathbf{z} , problem (1.22) can be relaxed into:

$$\min_{\mathbf{x}, \mathbf{z}} \lambda \|\mathbf{y} - \mathbf{S}\mathbf{F}\mathbf{x}\|_2^2 + \mu \|\mathbf{x} - \mathbf{z}\|_2^2 + \mathcal{R}(\mathbf{z}), \quad (1.23)$$

where $\mu > 0$ is the penalty parameter. When $\mu \rightarrow \infty$, the relaxed problem (1.23) reduces to the original one (1.22). Problem (1.23) can be solved by alternately minimizing over \mathbf{x} and \mathbf{z} :

$$\mathbf{z}_{k+1} \leftarrow \arg \min_{\mathbf{z}} \mathcal{R}(\mathbf{z}) + \mu \|\mathbf{x}_k - \mathbf{z}\|_2^2, \quad (1.24)$$

$$\begin{aligned} \mathbf{x}_{k+1} &\leftarrow \arg \min_{\mathbf{x}} \lambda \|\mathbf{y} - \mathbf{S}\mathbf{F}\mathbf{x}\|_2^2 + \mu \|\mathbf{x} - \mathbf{z}_{k+1}\|_2^2 \\ &= \mathbf{F}^H \mathbf{\Lambda} \mathbf{F} \mathbf{z}_k + \frac{\lambda_0}{1 + \lambda_0} \mathbf{S} \mathbf{F}^H \mathbf{y} \\ &:= \mathcal{DC}(\mathbf{z}_k; \mathbf{y}, \lambda_0, \Omega), \end{aligned} \quad (1.25)$$

where $\lambda_0 = \frac{\lambda}{\mu}$, $\mathbf{\Lambda}$ is a diagonal matrix accounting for the under-sampling scheme, and Ω is the index set of the acquired k -space samples. Qin *et al.* (Qin et al. 2018) propose to replace (1.24) with a CRNN, providing the following iterations:

$$\begin{aligned} \mathbf{z}_{k+1} &\leftarrow \mathbf{x}_k + \text{CRNN}(\mathbf{x}_k), \\ \mathbf{x}_{k+1} &\leftarrow \mathcal{DC}(\mathbf{z}_{k+1}; \mathbf{y}, \lambda_0, \Omega). \end{aligned}$$

The CRNN is a learnable RNN which integrates convolutions and evolves both over iterations and time. To this end, the authors introduce bidirectional convolutional recurrent units, evolving both over time and iterations, and convolutional recurrent units, evolving over iterations only. CRNN introduces inter-iteration connections so that information can be propagated across iterations, whereas in conventional unrolling techniques the iterations are typically disconnected. In addition, CRNN exploits temporal dependency and data redundancies of the dynamic MRI data by introducing temporal progressions. Different from typical RNNs, The weights for CRNN are independent across layers. The network is trained end-to-end by minimizing the MSE loss between the predicted MR images and ground truth data. Experimentally, CRNN achieves nearly 1dB improvement of PSNR for dynamic MRI, compared to state-of-the-art approaches

including both iterative reconstruction and deep learning. In terms of running time, it is also significantly faster than both classes of approaches.

In a different algorithmic front, Pramanik *et al.* (Pramanik, Aggarwal & Jacob 2020) unroll the Structured Low-Rank (SLR) algorithm for calibration-less parallel MRI and multishot MRI applications. The SLR algorithm performs MR image reconstruction by lifting the signal into a structured matrix and solving the following rank minimization problem:

$$\begin{aligned} \min_{\mathbf{\Gamma}} \quad & \text{rank} \left[\mathcal{T} \left(\mathcal{G} \left(\hat{\mathbf{\Gamma}} \right) \right) \right] \\ \text{subject to} \quad & \mathbf{B} = \mathcal{A}(\mathbf{\Gamma}) + \mathbf{P}, \end{aligned} \quad (1.26)$$

where $\mathbf{\Gamma}$ is the matrix representing multi-channel images on different coils, $\hat{\cdot}$ denotes the Discrete Fourier Transform (DFT), \mathbf{B} is the corresponding noisy under-sampled multi-channel Fourier measurement, \mathcal{A} is the linear operator formed by composing the Fourier transform with subsampling, and \mathbf{P} is the multi-channel noise matrix. Here \mathcal{G} is the mapping from Fourier samples to their gradients, and \mathcal{T} is the lifting operator that lifts the signal into a higher dimensional structured matrix. The low-rank constraint comes from the fact that the matrix $\mathcal{T} \left(\mathcal{G} \left(\hat{\mathbf{\Gamma}} \right) \right)$ has a high-dimensional null space, which in turns originates from sparsity of edges in natural images. For technical details, see (Pramanik et al. 2020) and (Ongie, Biswas & Jacob 2017).

Problem (1.26) is difficult to tackle directly due to its non-convex nature, and the following convex relaxation usually serves as a tractable surrogate:

$$\min_{\mathbf{\Gamma}} \quad \|\mathcal{A}(\mathbf{\Gamma}) - \mathbf{B}\|_2^2 + \lambda \left\| \mathcal{T} \left(\mathcal{G} \left(\hat{\mathbf{\Gamma}} \right) \right) \right\|_*, \quad (1.27)$$

where λ is the regularization coefficient and $\|\cdot\|_*$ is the nuclear norm whose minimization promotes low-rank structures of the solution. Problem (1.27) can be solved by the Iteratively Reweighted Least Squares (IRLS) algorithm which majorizes the nuclear norm with a weighted Frobenius norm and solves the problem:

$$\min_{\mathbf{\Gamma}, \mathbf{Q}} \quad \|\mathcal{A}(\mathbf{\Gamma}) - \mathbf{B}\|_2^2 + \lambda \left\| \mathcal{T} \left(\mathcal{G} \left(\hat{\mathbf{\Gamma}} \right) \right) \mathbf{Q} \right\|_F^2. \quad (1.28)$$

By introducing an auxiliary variable $\hat{\mathbf{Z}}$, problem (1.28) can be further relaxed into:

$$\min_{\mathbf{\Gamma}, \mathbf{Q}, \hat{\mathbf{Z}}} \quad \|\mathcal{A}(\mathbf{\Gamma}) - \mathbf{B}\|_2^2 + \lambda \left\| \mathcal{T} \left(\hat{\mathbf{Z}} \right) \mathbf{Q} \right\|_F^2 + \beta \left\| \mathcal{G} \left(\hat{\mathbf{\Gamma}} \right) - \hat{\mathbf{Z}} \right\|_2^2, \quad (1.29)$$

where $\beta > 0$ is the penalty coefficient. Problem (1.29) can be solved by alternately

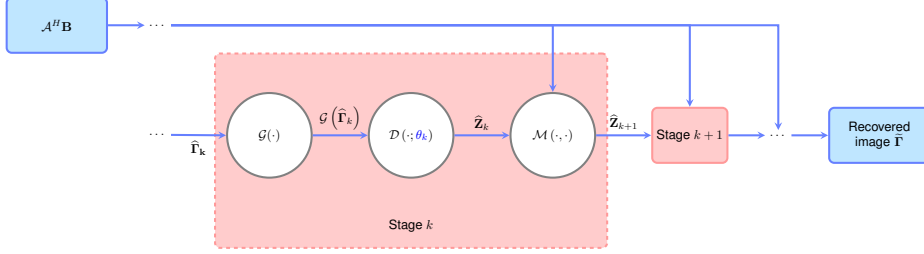


Figure 1.11 Diagram representation of DSLR (Pramanik et al. 2020): at each stage, the input $\hat{\Gamma}_k$ passes through a gradient operator, a CNN defined in (1.32), and a data consistency layer defined by (1.30). Trainable parameters are colored in blue.

minimizing over $\hat{\Gamma}$, $\hat{\mathbf{Z}}$ and \mathbf{Q} :

$$\begin{aligned} \hat{\Gamma}_{k+1} &\leftarrow \arg \min_{\hat{\Gamma}} \|\mathcal{A}(\hat{\Gamma}) - \mathbf{B}\|_2^2 + \beta \|\mathcal{G}(\hat{\Gamma}) - \hat{\mathbf{Z}}_k\|_2^2 \\ &= (\mathcal{A}^H \mathcal{A} + \beta \mathcal{G}^H \mathcal{G})^{-1} (\mathcal{A}^H \mathbf{B} + \beta \mathcal{G}^H (\hat{\mathbf{Z}}_k)) \\ &:= \mathcal{M}(\mathcal{A}^H \mathbf{B}, \mathbf{Z}_k) \end{aligned} \quad (1.30)$$

$$\begin{aligned} \hat{\mathbf{Z}}_{k+1} &\leftarrow \arg \min_{\hat{\mathbf{Z}}} \beta \|\mathcal{G}(\hat{\Gamma}_{k+1}) - \hat{\mathbf{Z}}\|_2^2 + \lambda \|\mathcal{T}(\hat{\mathbf{Z}}) \mathbf{Q}\|_F^2 \\ &= \left[\mathbf{I} + \frac{\lambda}{\beta} \mathcal{J}(\mathbf{Q}_k)^H \mathcal{J}(\mathbf{Q}_k) \right]^{-1} \mathcal{G}(\hat{\Gamma}_{k+1}), \end{aligned} \quad (1.31)$$

$$\mathbf{Q}_{k+1} = \left[\mathcal{T}(\mathcal{G}(\hat{\Gamma}_{k+1}))^H \mathcal{T}(\mathcal{G}(\hat{\Gamma}_{k+1})) + \epsilon_{k+1} \mathbf{I} \right]^{-\frac{1}{4}},$$

where \mathcal{J} is a lifting operator such that $\mathcal{J}(\mathbf{Q})$ represents a filter bank. Pramanik *et al.* (Pramanik et al. 2020) propose to replace the update step (1.31) with a denoising CNN, and thus adopt the following iteration procedures:

$$\begin{aligned} \hat{\mathbf{Z}}_k &\leftarrow \mathcal{D}[\mathcal{G}(\hat{\Gamma}_k); \theta_k], \\ \hat{\Gamma}_{k+1} &\leftarrow \mathcal{M}(\mathcal{A}^H \mathbf{B}, \mathbf{Z}_k), \end{aligned} \quad (1.32)$$

where $\mathcal{D}(\cdot; \theta_k)$ is a CNN with parameter θ_k . The unrolled network, called Deep SLR (DSLRL), is illustrated visually in Fig. 1.11. At implementation, DSLR adopts a hybrid regularization scheme, which incorporates an additional prior to exploit image-domain redundancies. Training is performed using the MSE loss.

Experimentally, DSLR demonstrates superior performance over state-of-the-art techniques on several evaluation metrics: SNR, PSNR, and SSIM. In addition, DSLR runs significantly faster compared with SLR methods as it is free from expensive operations such as Singular Value Decomposition (SVD), bringing down the running time from tens of minutes to less than a second. Figure 1.12 provides a visual comparison between DSLR and state-of-the-art MRI algorithms, where it is clearly observed that DSLR achieves much more accurate recovery with lower errors and higher quantitative scores.

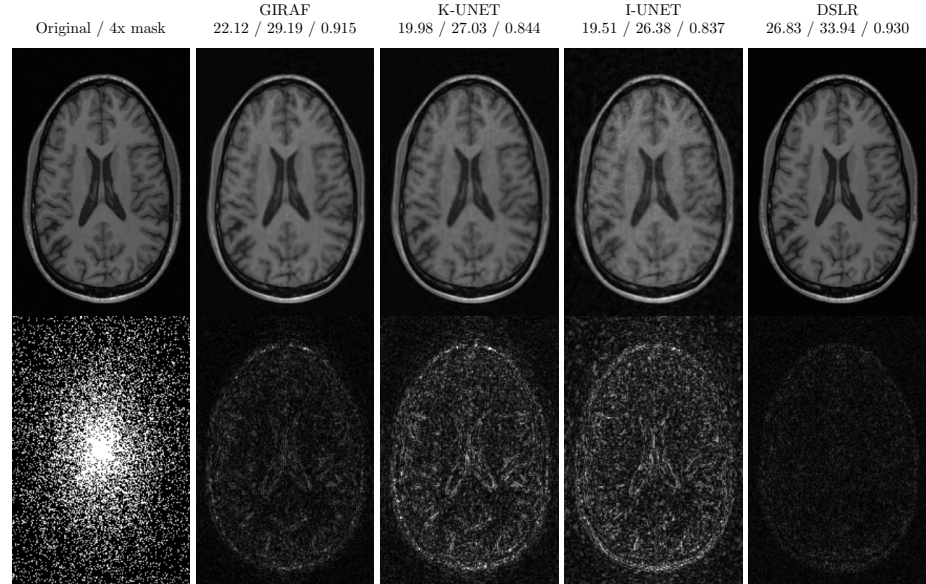


Figure 1.12 Experimental results on reconstruction of 4x accelerated single-channel brain data. The data was under-sampled using a Cartesian 2D non-uniform variable-density mask. The SNR (dB) / PSNR (dB) / SSIM values are also included for quantitative comparisons. The top row and the bottom row show reconstructed images (in magnitude) and corresponding error images, respectively. DSLRL is proposed in (Pramanik et al. 2020), while the SLR algorithm (GIRAF) (Ongie & Jacob 2017), k -space UNet (K-UNET) (Han et al. 2019) and image domain UNET (I-UNET) are state-of-the-art techniques for comparison. Images are courtesy of Matthews Jacob at University of Iowa (Pramanik et al. 2020).

1.3.5 Unrolling Techniques across Multiple Biomedical Imaging Modalities

In addition to application-specific approaches, there are numerous techniques applicable to multiple medical imaging modalities. Different medical imaging problems may share a similar forward model and have common prior structure, which enables the development of an abstract imaging algorithm that can be adapted towards each particular problem. An example that unrolls the well-known Alternating Direction Method of Multipliers (ADMM) algorithm is the ADMM-CSNet proposed in (Yang et al. 2018), where Yang *et al.* develop a Compressive Sensing (CS) technique for a linear imaging model. Specifically, the measurement vector $\mathbf{y} \in \mathbb{C}^m$ is collected through $\mathbf{y} \approx \mathbf{W}\mathbf{x}$ where $\mathbf{W} \in \mathbb{C}^{n \times m}$ is a measurement matrix with $m > n$ and $\mathbf{x} \in \mathbb{R}^m$ is the signal to be recovered.

The CS problem is typically solved by exploiting the underlying sparse structure of the signal \mathbf{x} in a certain transformation domain (Eldar & Kutyniok 2012b). In (Yang et al. 2018), a slightly generalized CS model is employed, which

amounts to solving the following optimization problem (Yang et al. 2018):

$$\min_{\mathbf{x}} \frac{1}{2} \|\mathbf{W}\mathbf{x} - \mathbf{y}\|_2^2 + \sum_{i=1}^C \lambda_i g(\mathbf{D}_i \mathbf{x}), \quad (1.33)$$

where λ_i 's are positive regularization coefficients, $g(\cdot)$ is a sparsity-inducing function, and $\{\mathbf{D}_i\}_{i=1}^C$ is a sequence of C operators, which effectively perform linear filtering operations. Concretely, \mathbf{D}_i can be taken as a wavelet transform and g can be chosen as the ℓ^1 norm. However, instead of resorting to analytical filters and prior functions, in (Yang et al. 2018) they are learned from training data through unrolling.

In general, there are numerous techniques for solving (1.33) such as the ISTA algorithm discussed in 1.2.1. Among them a simple yet efficient algorithm is ADMM (Boyd, Parikh, Chu, Peleato, Eckstein et al. 2011), which has found wide applications in various imaging domains. To employ it, problem (1.33) is first recast into a constrained minimization problem through variable splitting, by introducing variables $\{\mathbf{z}_i\}_{i=1}^C$:

$$\begin{aligned} \min_{\mathbf{x}, \{\mathbf{z}_i\}_{i=1}^C} \quad & \frac{1}{2} \|\mathbf{W}\mathbf{x} - \mathbf{y}\|_2^2 + \sum_{i=1}^C \lambda_i g(\mathbf{z}_i), \\ \text{subject to} \quad & \mathbf{z}_i = \mathbf{D}_i \mathbf{x}, \quad \forall i. \end{aligned} \quad (1.34)$$

The corresponding augmented Lagrangian is then formed as:

$$\mathcal{L}_\rho(\mathbf{x}, \mathbf{z}; \boldsymbol{\alpha}_i) = \frac{1}{2} \|\mathbf{W}\mathbf{x} - \mathbf{y}\|_2^2 + \sum_{i=1}^C \lambda_i g(\mathbf{z}_i) + \frac{\rho_i}{2} \|\mathbf{D}_i \mathbf{x} - \mathbf{z}_i + \boldsymbol{\alpha}_i\|_2^2, \quad (1.35)$$

where $\{\boldsymbol{\alpha}_i\}_{i=1}^C$ are the dual variables and $\{\rho_i\}_{i=1}^C$ are positive penalty coefficients. ADMM then alternately minimizes (1.35) followed by a dual variable update, leading to the following iterations:

$$\begin{aligned} \mathbf{x}^l &= \left(\mathbf{W}^H \mathbf{W} + \sum_{i=1}^C \rho_i \mathbf{D}_i^T \mathbf{D}_i \right)^{-1} \left[\mathbf{W}^H \mathbf{y} + \sum_{i=1}^C \rho_i \mathbf{D}_i^T (\mathbf{z}_i^{l-1} - \boldsymbol{\alpha}_i^{l-1}) \right] \\ &:= \mathcal{U}^1 \{ \mathbf{y}, \boldsymbol{\alpha}_i^{l-1}, \mathbf{z}_i^{l-1}, \rho_i, \mathbf{D}_i \}, \\ \mathbf{z}_i^l &= \mathcal{P}_g \left\{ \mathbf{D}_i \mathbf{x}^l + \boldsymbol{\alpha}_i^{l-1}, \frac{\lambda_i}{\rho_i} \right\} \\ &:= \mathcal{U}^2 \{ \boldsymbol{\alpha}_i^{l-1}, \mathbf{x}^l; \lambda_i, \rho_i, \mathbf{D}_i \}, \\ \boldsymbol{\alpha}_i^l &= \boldsymbol{\alpha}_i^{l-1} + \eta_i (\mathbf{D}_i \mathbf{x}^l - \mathbf{z}_i^l) \\ &:= \mathcal{U}^3 \{ \boldsymbol{\alpha}_i^{l-1}, \mathbf{x}^l, \mathbf{z}_i^l; \eta_i, \mathbf{D}_i \}, \quad \forall i, \end{aligned} \quad (1.36)$$

where η_i 's are constant parameters, and $\mathcal{P}_g\{\cdot; \lambda\}$ is the proximal mapping for g with parameter λ . The unrolled network can thus be constructed by concatenating these operations. The parameters $\lambda_i, \rho_i, \eta_i, \mathbf{D}_i$ in each layer will be learned from real datasets. Fig. 1.13 depicts the resulting network architecture. In (Yang

et al. 2018) the authors discuss several implementation issues, including efficient matrix inversion and the analytic back-propagation rules. The network is trained by minimizing a normalized version of the Root-Mean-Square-Error (RMSE).

ADMM-CSNet demonstrates its efficacy through various experiments. In particular, for MRI applications, ADMM-CSNet achieves the same reconstruction accuracy using 10% less sampled data and speeds up recovery by around 40 times compared to conventional iterative methods. When compared with state-of-the-art deep networks, it exceeds their performance by a margin of around 3dB PSNR under 20% sampling rate on brain data.

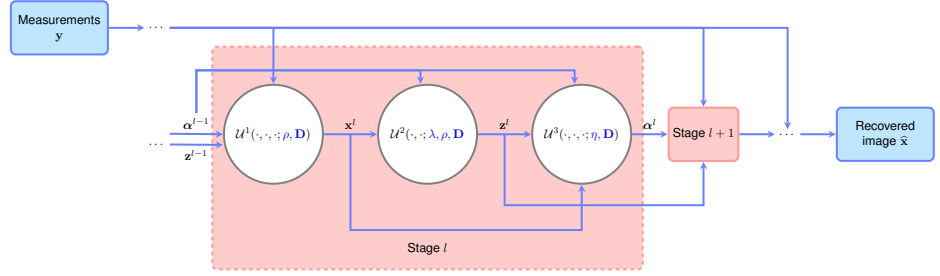


Figure 1.13 Diagram representation of ADMM-CSNet (Yang et al. 2018): each stage comprises a series of inter-related operations, whose analytic forms are given in (1.36). The trainable parameters are colored in blue.

In a similar fashion, Aggarwal *et al.* (Aggarwal, Mani & Jacob 2019) unrolls an alternating minimization algorithm over a regularized image reconstruction problem. By integrating a CNN into the image prior, they start with the following optimization problem:

$$\min_{\mathbf{x}} \|\mathbf{W}\mathbf{x} - \mathbf{y}\|_2^2 + \lambda \|\mathbf{x} - \mathcal{D}_\theta(\mathbf{x})\|_2^2, \quad (1.37)$$

where $\mathbf{x} \in \mathbb{C}^m$ is the underlying image to be recovered, $\mathbf{y} \in \mathbb{C}^n$ is the measurement vector, $\mathbf{W} \in \mathbb{C}^{n \times m}$ is the measurement model matrix, and \mathcal{D}_θ is a denoising CNN carrying parameters θ . Aggarwal *et al.* propose to solve (1.37) via the following iterations:

$$\begin{aligned} \mathbf{z}_k &\leftarrow \mathcal{D}_\theta(\mathbf{x}_k), \\ \mathbf{x}_{k+1} &\leftarrow \arg \min_{\mathbf{x}} \|\mathbf{W}\mathbf{x} - \mathbf{y}\|_2^2 + \lambda \|\mathbf{x} - \mathbf{z}_k\|_2^2 \\ &= (\mathbf{W}^H \mathbf{W} + \lambda \mathbf{I})^{-1} (\mathbf{W}^H \mathbf{y} + \lambda \mathbf{z}_k), \end{aligned} \quad (1.38)$$

where $\mathbf{I} \in \mathbb{R}^{m \times m}$ is the identity matrix. The network parameters θ are shared across different iterations. The unrolled network, dubbed MoDL, has a very similar structure to DSLR in Fig. 1.11. Training of MoDL is conducted by minimizing the MSE loss.

For applications such as MRI, \mathbf{W} corresponds to a composition of the sampling operator with the Fourier matrix and thus the iteration step (1.38) admits

a simple analytic formula. However, in more complex cases, such as multichannel MRI, the operator $\mathbf{W}^H\mathbf{W} + \lambda\mathbf{I}$ is not analytically invertible and iterative numerical methods such as Conjugate Gradient (CG) need to be plugged into the network. Aggrawal *et al.* (Aggarwal et al. 2019) verify that, although CG is an iterative technique, the intermediate results need not be stored to perform back-propagation. Instead, another CG step simply needs to be applied in the back-propagation step.

Numerous experiments verify the effectiveness of MoDL. When compared to other deep learning frameworks, MoDL achieves nearly 3dB higher PSNR values for 6x acceleration on their own dataset acquired through 3D T2 CUBE. Furthermore, as MoDL incorporates the forward model $\mathbf{y} = \mathbf{W}\mathbf{x}$, it is relatively insensitive to the undersampling patterns in MRI. In particular, when trained on 10x acceleration setting, MoDL is capable of faithfully recovering the images under 12x and 14x acceleration settings.

1.4 Perspectives and Recent Trends

We have so far reviewed several successes of algorithm unrolling, including both conceptual and practical breakthroughs in many biomedical imaging topics. In this section we will put algorithm unrolling into perspective, in order to understand why it is beneficial compared with traditional iterative algorithms and contemporary DNNs. Furthermore, we summarize some recent trends that we observe in many biomedical imaging works.

1.4.1 Why is Unrolling So Effective for Biomedical Imaging?

In recent years, algorithm unrolling has proved highly effective in achieving superior performance and higher efficiency in many practical domains, while inheriting interpretability from the underlying iterative algorithms. In addition, it frequently demonstrates improved robustness under deviations of training data and forward models compared with generic DNNs. A question that naturally arises is, why is it so powerful?

From a machine learning perspective, a fundamental trade-off for learning-based models is the *bias-variance trade-off* (Friedman, Hastie, Tibshirani et al. 2001). Models that have low capacity, such as linear models, typically generalize better but may prove inadequate to capture complicated data patterns. Such models generally exhibit high bias and low variance. In contrast, models that have abundant capacity, such as DNNs, are capable of fitting sophisticated functions but have high risk of overfitting.

Unrolled networks achieve a more favorable bias-variance trade-off compared with alternative techniques (Yang et al. 2018), in particular generic neural networks and iterative algorithms. Fig. 1.14 provides a high-level illustration of the

representation capability of these classes of techniques, from a functional approximation perspective. The area of various class of methods represents their capability in fitting functions, i.e., their modeling capacity as functional approximators. A traditional iterative algorithm spans a relatively small subset of the functions compared to deep learning techniques, and thus has low variance but high bias. Indeed, in practice iterative algorithms typically underperform deep learning techniques which provides as a strong evidence of their low modeling capacity. Therefore, there is generally an irreducible gap between its spanned set and the target function. Nevertheless, in implementing iterative methods, typically the user tweaks the architecture and fine-tunes parameters, rendering it capable of approximating a given target function reasonably well and effectively reducing the gap. On the other hand, iterative algorithms generalize relatively well in limited training scenarios thanks to their low variance. In biomedical imaging, the data is generally difficult to gather due to high costs of imaging devices and requirements of patients. Therefore, iterative algorithms have played a critical role for many years.

On the other hand, a generic neural network is capable of more accurately approximating the target function thanks to its universal approximation capability (Sonoda & Murata 2017). As shown in Fig. 1.14, it constitutes a large subset in the function space. In practice, it has been empirically supported that DNNs can approximate complicated mappings as long as the data is sufficient. Nowadays, DNNs typically consists of an enormous number of parameters and have low bias but high variance. The high dimensionality of parameters requires abundant training samples, otherwise generalization becomes a serious issue. Furthermore, searching for the target function out of its huge spanned space is rather difficult which poses great challenges in training.

In contrast, the unrolled networks are typically constructed by expanding the capacity of iterative algorithms, through generalizations of the underlying iterations. Therefore, it integrates domain knowledge from iterative algorithms and can approximate the target function more accurately, while spanning a relatively small subset in the function space. Reduced size of the search space alleviates the burden of training and requirement of large scale training datasets. In addition, unrolled networks have better generalizability thanks to their lower variance and are less prone to overfitting. As an intermediate model between generic networks and iterative algorithms, unrolled networks typically have relatively low bias and variance simultaneously.

1.4.2 Emerging Unrolling Trends for Biomedical Imaging

As we have seen through various case studies, there are a few common trends shared by many methods, which are summarized below.

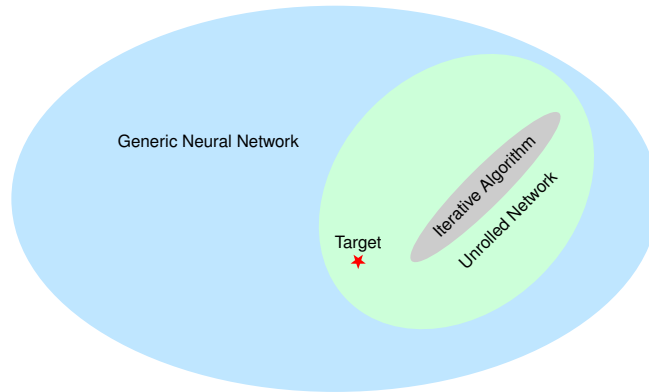


Figure 1.14 A high-level unified interpretation of algorithm unrolling from a functional approximation perspective: the ellipses depict the scope of functions that can be approximated by each category of methods. Compared with iterative algorithms which have limited representation power and usually underfit the target, unrolled networks often better approximate the target thanks to their higher representation power. On the other hand, unrolled networks have lower representation power than generic neural networks but usually generalize better in practice, hence providing an attractive balance.

Using DNNs as learnable operators

As discussed in Section 1.2, an important procedure in constructing unrolled networks is to generalize the functional form per iteration. A commonly employed technique is to substitute certain operators with DNNs. In particular, proximal operators which manifest in various regularized inverse problems are frequently replaced by parameterized deep networks such as CNNs (Gupta et al. 2018, Hauptmann et al. 2018, Adler & Öktem 2018) or RNNs (Qin et al. 2018). This substitution technique is reminiscent of the Plug-and-Play scheme (Ahmad, Bouman, Buzzard, Chan, Liu, Reehorst & Schniter 2020), where the proximal operators are replaced with an off-the-shelf image denoiser such as Block-Matching and 3D filtering (BM3D) (Dabov, Foi, Katkovnik & Egiazarian 2007).

Exploring broader classes of algorithms

In the early stage of unrolling research the focus was primarily in unrolling ISTA-like algorithms (Gregor & LeCun 2010, Jin et al. 2017). Nowadays, researchers are pursuing other alternatives such as PGD (Gupta et al. 2018), ADMM (Yang et al. 2018), and IRLS (Pramanik et al. 2020), to name a few. This trend has contributed greatly to the novelty and variety of unrolling approaches.

Balancing performance and efficiency trade-offs

In practice, when designing unrolled deep networks, there is a fundamental trade-off between performance and efficiency: wider and deeper networks with numerous parameters generally achieve better performance but are usually less efficient

and more data demanding. Therefore, under practical constraints important design choices have to be made. One distinction is whether to use shared parameters across all the layers or adopt layer-specific parameters. Another issue is how to determine the depth of the networks, i.e., number of iterations in the algorithm.

1.5 Conclusions

In this chapter we discussed algorithm unrolling, a systematic approach to construct deep networks out of iterative algorithms, and its applications to biomedical imaging. We first provided a comprehensive tutorial on algorithm unrolling and how to leverage it to construct deep networks. We then showcased how algorithm unrolling can be applied in biomedical imaging by discussing concrete examples in different medical imaging modalities. We next put algorithm unrolling into perspective, illustrated why it can be so powerful from a bias-variance trade-off standpoint, and summarized several recent trends in unrolling research.

To facilitate future research, we conclude this chapter by briefly discussing open challenges and suggesting possible future research directions. First, although algorithm unrolling has inherited the merits of iterative algorithms to a large extent, customizations of the iteration procedures might undermine some of them. In particular, convergence guarantees may no longer hold. Therefore, it is interesting to extend the theories around iterative algorithms to incorporate interesting unrolled networks. Second, as algorithm unrolling serves as a valuable bridge between iterative algorithms and deep networks, it can be regarded as a tool to understand why deep networks are so effective in practical imaging applications, in order to complement their lack of interpretability. Finally, in biomedical imaging training data is relatively deficient. Since algorithm unrolling has already demonstrated superior generalizability in many previous works, it is interesting to exploit it as a viable alternative under limited training scenarios, in addition to and/or integrated with semi-supervised learning.

References

- Adler, J. & Öktem, O. (2018), ‘Learned Primal-dual Reconstruction’, *IEEE Trans. Med. Imag.* **37**(6), 1322–1332.
- Aggarwal, H. K., Mani, M. P. & Jacob, M. (2019), ‘MoDL: Model-Based Deep Learning Architecture for Inverse Problems’, *IEEE Trans. Med. Imag.* **38**(2), 394–405.
- Ahmad, R., Bouman, C. A., Buzzard, G. T., Chan, S., Liu, S., Reehorst, E. T. & Schniter, P. (2020), ‘Plug-and-play Methods for Magnetic Resonance Imaging: Using Denoisers for Image Recovery’, *IEEE Signal Process. Mag.* **37**(1), 105–116.
- Bar-Shira, O., Grubstein, A., Rapson, Y., Suhami, D., Atar, E., Peri-Hanania, K., Rosen, R. & Eldar, Y. C. (2021), ‘Learned super resolution ultrasound for improved breast lesion characterization’, *arXiv preprint arXiv:2107.05270*.
- Boyd, S., Parikh, N., Chu, E., Peleato, B., Eckstein, J. et al. (2011), ‘Distributed Optimization and Statistical Learning via the Alternating Direction Method of Multipliers’, *Found. Trends[®] Mach. Learn.* **3**(1), 1–122.
- Chen, S. S., Donoho, D. L. & Saunders, M. A. (2001), ‘Atomic Decomposition by Basis Pursuit’, *SIAM review* **43**(1), 129–159.
- Chen, X., Liu, J., Wang, Z. & Yin, W. (2018), Theoretical Linear Convergence of Unfolded ISTA and Its Practical Weights and Thresholds, *in* ‘Adv. Neural Inform. Process. Syst.’.
- Chun, I. Y., Zheng, X., Long, Y. & Fessler, J. A. (2019), Bcd-net for Low-dose CT Reconstruction: Acceleration, Convergence, and Generalization, *in* ‘Int. Conf. Med. Image Comput. Computer-Assist. Intervent.’, Springer, pp. 31–40.
- Chun, Y. & Fessler, J. A. (2018), Deep BCD-net Using Identical Encoding-decoding CNN Structures for Iterative Image Recovery, *in* ‘IEEE Image, Video, and Multidimensional Signal Processing Workshop (IVMSP)’, IEEE, pp. 1–5.
- Dabov, K., Foi, A., Katkovich, V. & Egiazarian, K. (2007), ‘Image Denoising by Sparse 3D Transform-domain Collaborative Filtering’, *IEEE Trans. Image Process.* **16**(8), 2080–2095.
- Dardikman-Yoffe, G. & Eldar, Y. C. (2020), ‘Learned SPARCOM: Unfolded Deep Super-resolution Microscopy’, *Opt. Express* **28**(19), 27736–27763.
- Daubechies, I., Defrise, M. & De Mol, C. (2004), ‘An Iterative Thresholding Algorithm for Linear Inverse Problems with a Sparsity Constraint’, *Commun. Pure Appl. Math.* **57**(11), 1413–1457.
- Doneva, M. (2020), ‘Mathematical Models for Magnetic Resonance Imaging Reconstruction: An Overview of the Approaches, Problems, and Future Research Areas’, *IEEE Signal Process. Mag.* **37**(1), 24–32.

- Dong, B., Jiang, Q. & Shen, Z. (2017), ‘Image restoration: Wavelet frame shrinkage, nonlinear evolution pdes, and beyond’, *Multiscale Modeling & Simulation* **15**(1), 606–660.
- Eldar, Y. C. & Kutyniok, G. (2012a), *Compressed Sensing: Theory and Applications*, Cambridge university press.
- Eldar, Y. C. & Kutyniok, G. (2012b), *Compressed Sensing: Theory and Applications*, Cambridge university press.
- Friedman, J., Hastie, T., Tibshirani, R. et al. (2001), *The Elements of Statistical Learning*, Vol. 1, Springer series in statistics New York.
- Furlow, B. (2009), ‘Contrast-enhanced Ultrasound’, *Radiologic technology* **80**(6), 547S–561S.
- Gregor, K. & LeCun, Y. (2010), Learning Fast Approximations of Sparse Coding, in ‘Proc. Int. Conf. Mach. Learn.’.
- Gupta, H., Jin, K. H., Nguyen, H. Q., McCann, M. T. & Unser, M. (2018), ‘CNN-based Projected Gradient Descent for Consistent CT Image Reconstruction’, *IEEE Trans. Med. Imag.* **37**(6), 1440–1453.
- Han, Y., Sunwoo, L. & Ye, J. C. (2019), ‘ k -Space Deep Learning for Accelerated MRI’, *IEEE Trans. Med. Imag.* **39**(2), 377–386.
- Hauptmann, A., Lucka, F., Betcke, M., Huynh, N., Adler, J., Cox, B., Beard, P., Ourselin, S. & Arridge, S. (2018), ‘Model-based Learning for Accelerated, Limited-view 3D Photoacoustic Tomography’, *IEEE Trans. Med. Imag.* **37**(6), 1382–1393.
- Huang, B. (2010), ‘Super-resolution Optical Microscopy: Multiple Choices’, *Curr. Opin. Chem. Biol.* **14**(1), 10–14.
- Jin, K. H., McCann, M. T., Froustey, E. & Unser, M. (2017), ‘Deep Convolutional Neural Network for Inverse Problems in Imaging’, *IEEE Trans. Image Process.* **26**(9), 4509–4522.
- Kang, E., Chang, W., Yoo, J. & Ye, J. C. (2018), ‘Deep Convolutional Framelet Denosing for Low-dose CT via Wavelet Residual Network’, *IEEE Trans. Med. Imag.* **37**(6), 1358–1369.
- LeCun, Y. A., Bottou, L., Orr, G. B. & Müller, k. (2012), Efficient BackProp, in ‘Neural Networks: Tricks of the Trade’, Lect. Notes Comput. Sci., Springer, Berlin, Heidelberg, pp. 9–48.
- Li, M., Fan, Z., Ji, H. & Shen, Z. (2014), ‘Wavelet frame based algorithm for 3d reconstruction in electron microscopy’, *SIAM Journal on Scientific Computing* **36**(1), B45–B69.
- Liu, J., Chen, X., Wang, Z. & Yin, W. (2019), ALISTA: Analytic Weights Are As Good As Learned Weights in LISTA, in ‘Proc. Int. Conf. Learn. Representation’.
- Min, S., Lee, B. & Yoon, S. (2017), ‘Deep Learning in Bioinformatics’, *Brief. Bioinform.* **18**(5), 851–869.
- Mischi, M., Bell, M. A. L., van Sloun, R. J. & Eldar, Y. C. (2020), ‘Deep learning in medical ultrasound—from image formation to image analysis’, *IEEE Trans. Ultrason. Ferroelectr. Freq. Control.* **67**(12), 2477–2480.
- Monga, V., Li, Y. & Eldar, Y. C. (2019), ‘Algorithm unrolling: Interpretable, efficient deep learning for signal and image processing’, *arXiv preprint arXiv:1912.10557*.
- Nehme, E., Weiss, L. E., Michaeli, T. & Shechtman, Y. (2018), ‘Deep-STORM: Super-resolution Single-molecule Microscopy by Deep Learning’, *Optica* **5**(4), 458–464.

- Ongie, G., Biswas, S. & Jacob, M. (2017), ‘Convex Recovery of Continuous Domain Piecewise Constant Images from Nonuniform Fourier Samples’, *IEEE Trans. Signal Process.* **66**(1), 236–250.
- Ongie, G. & Jacob, M. (2017), ‘A Fast Algorithm for Convolutional Structured Low-rank Matrix Recovery’, *IEEE Trans. Comput. Imag.* **3**(4), 535–550.
- Pramanik, A., Aggarwal, H. & Jacob, M. (2020), ‘Deep Generalization of Structured Low-Rank Algorithms (Deep-SLR)’, *IEEE Trans. Med. Imag.* .
- Qin, C., Schlemper, J., Caballero, J., Price, A. N., Hajnal, J. V. & Rueckert, D. (2018), ‘Convolutional Recurrent Neural Networks for Dynamic MR Image Reconstruction’, *IEEE Trans. Med. Imag.* **38**(1), 280–290.
- Rockafellar, R. T. (1970), *Convex Analysis*, Vol. 36, Princeton university press.
- Ronneberger, O., Fischer, P. & Brox, T. (2015), U-net: Convolutional Networks for Biomedical Image Segmentation, in ‘Int. Conf. Med. Image Comput. Comput. Assist. Interv.’, pp. 234–241.
- Solomon, O., Cohen, R., Zhang, Y., Yang, Y., He, Q., Luo, J., van Sloun, R. J. G. & Eldar, Y. C. (2020), ‘Deep Unfolded Robust PCA with Application to Clutter Suppression in Ultrasound’, *IEEE Trans. Med. Imag.* **39**(4), 1051–1063.
- Solomon, O., Eldar, Y. C., Mutzafi, M. & Segev, M. (2019), ‘SPARCOM: Sparsity based Super-resolution Correlation Microscopy’, *SIAM J. Imaging Sci.* **12**(1), 392–419.
- Sonoda, S. & Murata, N. (2017), ‘Neural Network with Unbounded Activation Functions is Universal Approximator’, *Applied and Computational Harmonic Analysis* **43**(2), 233–268.
- Van Sloun, R. J., Cohen, R. & Eldar, Y. C. (2019), ‘Deep learning in ultrasound imaging’, *Proceedings of the IEEE* **108**(1), 11–29.
- Wang, Z., Liu, D., Yang, J., Han, W. & Huang, T. (2015), Deep Networks for Image Super-Resolution with Sparse Prior, in ‘Proc. IEEE Int. Conf. Comput. Vis.’, pp. 370–378.
- Wu, D., Kim, K., Dong, B., Fakhri, G. E. & Li, Q. (2018), End-to-End Lung Nodule Detection in Computed Tomography, in ‘Machine Learning in Medical Imaging’, Lect. Notes Comput. Sci., Springer International Publishing, Cham, pp. 37–45.
- Xin, B., Wang, Y., Gao, W., Wipf, D. & Wang, B. (2016), Maximal Sparsity with Deep Networks?, in ‘Adv. Neural Inform. Process. Syst.’, pp. 4340–4348.
- Yang, Y., Sun, J., Li, H. & Xu, Z. (2018), ‘ADMM-CSNet: A Deep Learning Approach for Image Compressive Sensing’, *IEEE Trans. Pattern Anal. Mach. Intell.* .
- Ye, J. C., Han, Y. & Cha, E. (2018), ‘Deep Convolutional Framelets: A General Deep Learning Framework for Inverse Problems’, *SIAM J. Imaging Sci.* **11**(2), 991–1048.
- Zhang, X.-P. (2001), ‘Thresholding neural network for adaptive noise reduction’, *IEEE transactions on neural networks* **12**(3), 567–584.